

Waveform Modeling of the Crust and Upper Mantle Using S, Sp, SsPmP, and Shear-Coupled PL Waves

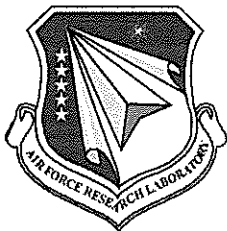
**Jay Pulliam
Mrinal K. Sen
Abhijit Gangopadhyay**

**University of Texas at Austin
Institute for Geophysics, Building 196
J.J. Pickle Research Campus
10100 Burnet Road
Austin, TX 78758**

Final Report

10 May 2008

APPROVED FOR PUBLIC RELEASE; DISTRIBUTION UNLIMITED.



**AIR FORCE RESEARCH LABORATORY
Space Vehicles Directorate
29 Randolph Road
AIR FORCE MATERIEL COMMAND
Hanscom AFB, MA 01731-3010**

NOTICE AND SIGNATURE PAGE

Using Government drawings, specifications, or other data included in this document for any purpose other than Government procurement does not in any way obligate the U.S. Government. The fact that the Government formulated or supplied the drawings, specifications, or other data does not license the holder or any other person or corporation; or convey any rights or permission to manufacture, use, or sell any patented invention that may relate to them.

This report was cleared for public release and is available to the general public, including foreign nationals. Qualified requestors may obtain additional copies from the Defense Technical Information Center (DTIC) (<http://www.dtic.mil>). All others should apply to the National Technical Information Service.

AFRL-RV-HA-TR-2008-1052 HAS BEEN REVIEWED AND IS APPROVED FOR
PUBLICATION IN ACCORDANCE WITH ASSIGNED DISTRIBUTION STATEMENT.

//Signature//

ROBERT RAISTRICK
Contract Manager

//Signature//

PAUL TRACY, Acting Chief
Battlespace Surveillance Innovation Center

This report is published in the interest of scientific and technical information exchange, and its publication does not constitute the Government's approval or disapproval of its ideas or findings.

REPORT DOCUMENTATION PAGE				Form Approved OMB No. 0704-0188	
Public reporting burden for this collection of information is estimated to average 1 hour per response, including the time for reviewing instructions, searching existing data sources, gathering and maintaining the data needed, and completing and reviewing this collection of information. Send comments regarding this burden estimate or any other aspect of this collection of information, including suggestions for reducing this burden to Department of Defense, Washington Headquarters Services, Directorate for Information Operations and Reports (0704-0188), 1215 Jefferson Davis Highway, Suite 1204, Arlington, VA 22202-4302. Respondents should be aware that notwithstanding any other provision of law, no person shall be subject to any penalty for failing to comply with a collection of information if it does not display a currently valid OMB control number. PLEASE DO NOT RETURN YOUR FORM TO THE ABOVE ADDRESS.					
1. REPORT DATE (DD-MM-YYYY) 20 May 2008		2. REPORT TYPE Final Report		3. DATES COVERED (From - To) 01-10-2004 to 30-09-2007	
4. TITLE AND SUBTITLE Waveform Modeling of the Crust and Upper Mantle Using S, Sp, SsPmP, and Shear-Coupled PL Waves				5a. CONTRACT NUMBER FA8718-04-C-0014	
				5b. GRANT NUMBER	
				5c. PROGRAM ELEMENT NUMBER 62601F	
6. AUTHOR(S) Jay Pulliam, Mrinal K. Sen, and Abhijit Gangopadhyay				5d. PROJECT NUMBER 1010	
				5e. TASK NUMBER SM	
				5f. WORK UNIT NUMBER A1	
7. PERFORMING ORGANIZATION NAME(S) AND ADDRESS(ES) University of Texas at Austin, Institute for Geophysics, J.J. Pickle Research Campus, Bldg. 196, 10100 Burnet Road, Austin, TX 78758				8. PERFORMING ORGANIZATION REPORT NUMBER	
9. SPONSORING / MONITORING AGENCY NAME(S) AND ADDRESS(ES) Air Force Research Laboratory 29 Randolph Rd. Hanscom AFB, MA 01731-3010				10. SPONSOR/MONITOR'S ACRONYM(S) AFRL/RVBYE	
				11. SPONSOR/MONITOR'S REPORT NUMBER(S) AFRL-RV-HA-TR-2008-1052	
12. DISTRIBUTION / AVAILABILITY STATEMENT Approved for Public Release; Distribution Unlimited.					
13. SUPPLEMENTARY NOTES					
14. ABSTRACT We developed a waveform modeling code that computes synthetic seismograms with a parallelized reflectivity method and fits the observed waveforms by global optimization. Assuming a 1-D, isotropic, layered Earth, our code computes synthetic seismograms for all layers, frequencies, and ray parameters. It implements a global optimization algorithm using Very Fast Simulated Annealing that allows for broad model space search so as to find the global minimum, and hence minimizes dependency on the starting model. Our method also computes the Posterior Probability Densities and correlation matrices to evaluate the uniqueness of the resulting models and trade-offs between individual model parameters. We applied the code to determine the crust and upper mantle structure beneath permanent broadband seismic stations in Africa, China, and Canada using large teleseismic earthquakes recorded at these stations. We modeled the S, Sp, SsPmP, and shear-coupled PL waves from these earthquakes and our P- and S-wave velocity models compare well with, and in some cases improve upon the models obtained from other existing methods. Our use of the shear-coupled PL phase wherever available improved constraints on the models of the lower crust and upper mantle.					
15. SUBJECT TERMS Waveform Modeling, Reflectivity Method, Global Optimization, Very Fast Simulated Annealing					
16. SECURITY CLASSIFICATION OF:			17. LIMITATION OF ABSTRACT SAR	18. NUMBER OF PAGES 46	19a. NAME OF RESPONSIBLE PERSON Robert Raistrick
a. REPORT UNCLASSIFIED	b. ABSTRACT UNCLASSIFIED	c. THIS PAGE UNCLASSIFIED			19b. TELEPHONE NUMBER (include area code) 781-377-3726

Table of Contents

1. Summary	1
2. Introduction	1
3. Methodology	2
3.1. Teleseismic Phases Modeled	
3.2. Waveform Modeling	4
3.3. Estimation of Uncertainties	6
4. Results and Discussion – Applications of the Method	8
4.1. Africa	9
4.2. China	19
4.3. Canada	24
5. Conclusions	28
References	31
List of Symbols, Abbreviations, and Acronyms	35

Figures

Figure 1: (a) Typical ray paths for S (path A-B), Sp (path P-N-B), and SsPmP (path Q-M-N-B) phases (Modified from Pulliam and Sen, 2005) (b) Propagation characteristics and excitation of shear-coupled PI waves with distance and corresponding phase velocity (V_{ph})-period (T) curve: α_N and β_N are the P and S wave velocities at the Moho, and c_1 , c_2 , and c_3 are the corresponding phase velocities as indicated (Modified from Baag and Langston, 1985).....3

Figure 1: (c) Three-component synthetic seismograms generated by the parallelized reflectivity program used in this study, using PREM as the velocity model, and for a teleseismic source located at an epicentral distance of 50° and focal depth of 600 km. The onset of the S, Sp, SsPmP, and SPL phases are indicated on the radial component seismogram (Modified from Pulliam and Sen, 2005).....4

Figure 2: Flow-chart elaborating the Very Fast Simulated Annealing (VFSA) algorithm used in this study for the waveform inversion by global optimization (Modified from Sen and Stoffa, 1995). $E(m^0)$ – error function for the initial model m^0 . $E(m^{new})$ – error function for the new model m^{new} , T = temperature, $r(T)$ – temperature dependent Cauchy-like distribution.....6

Figure 3: Map showing locations of the earthquakes used in this study (blue stars) and the permanent broadband seismic stations in the African continent (red triangles) that have recorded these earthquakes. The respective station codes are shown adjacent to each seismic station.....10

Figure 4: (a) Vertical and radial component seismograms for three events recorded at TAM showing the observed (solid line) and synthetic (dashed line) waveforms. The correlated waveforms are indicated on the panels. (b) Particle motion diagrams for a 10-s time window around the SPL arrivals for event 3 showing the diagnostic prograde elliptical motion of the SPL phase. The dotted portions of the diagrams indicate the beginning of the motion.....10

Figure 4: (c) P- and S-wave velocity models up to 100 km for station TAM from the inversion results for individual events recorded at TAM. (d) Model parameter correlation matrices for events 1 (left-hand panel) and 3 (right-hand panel) recorded at TAM. Each small square represents a model parameter (V_p , V_s , Thickness of layer, and Density) on both the horizontal and vertical axes. The correlations range between -1 and 1. Sparse colored squares off-diagonal in the lower crust-upper mantle in event 3 (right-hand panel) compared to that in event 1 (left-hand panel) indicate better resolution and confidence (less trade-off) in this region.....11

Figure 5: Preferred P- and S-wave velocity models for (a) TAM (b) DBIC (c) MBO and (d) MDT. The P- and S-wave velocity models (broken lines) in (a), (b), and (d) are from receiver function studies by Sandvol et al. (1998). The dotted lines in (a) show the P- and S-wave velocity model for TAM within \pm two standard errors.....14

Figure 6: (a) Obtained velocity model from this study (solid line) up to 30 km for station ATD and available velocity model from Sandvol et al. (1998) (broken line). Posterior Probability Distribution (b) and parameter correlation matrix (c) for event 13 recorded at ATD showing the tradeoffs between different model parameters in different layers. (d) Obtained velocity model from this study (solid line) up to 100 km for station FURI and available velocity model from Ayele et al. (2004) (broken line). Preferred P- and S-wave velocity models for (e) KMBO up to a depth of 50 km, and (f) MBAR up to a depth of 100 km.....16

Figure 7: Obtained P- and S-wave velocity models for (a) TSUM (b) LSZ and (c) LBTB. The P- and S-wave velocity models (broken lines) in (b) and (c) are from receiver function studies by Midzi and Ottemoller (2001).....18

Figure 8: Map showing earthquakes analyzed in this study (blue stars) and the permanent broadband seismic stations in China (red triangles) that recorded them. The respective station codes are shown adjacent to location of each station.....20

Figure 9: Vertical and radial component seismograms for example events recorded at LSA, WMQ, and BJT showing the observed (solid line) and synthetic (dashed line) waveforms. The correlated waveforms are indicated on the panels.....20

Figure 10: Posterior Probability Distribution (PPD) for example events recorded at (a) LSA and (c) WMQ. More peaked distributions indicate more uniqueness among different models and fewer trade-offs among model parameters. Model parameter correlation matrices for the same event at (b) LSA and (d) WMQ are also shown. Each small square represents a model parameter (V_p , V_s , Thickness of Layer, and Density) on both axes. The correlations range between -1 and 1. Sparse colored squares off-diagonal indicate better constraints and greater confidence (less trade-offs) in those parts of the models. Note that at LSA where we observe and match the SPL phase there are less colored squares in the correlation matrix in the lower crust-upper mantle (b) compared to that at WMQ (d), suggesting that SPL improves constraints in those parts of the models.....21

Figure 11: Obtained P- and S-wave velocity models (solid lines) for the eleven permanent broadband seismic stations in China. Station codes are indicated in each panel. The models (broken lines) in LZH, BJT, HIA, MDJ, WMQ, and KMI are from receiver function studies by Mangino et al. (1999).....23

Figure 12: Map showing earthquakes analyzed in this study (blue stars) and the permanent broadband seismic stations in Canada (red triangles) that recorded them. The respective station codes are shown adjacent to location of each station.....24

Figure 13: (a) Vertical and radial component seismograms for example events recorded at INK, LLLB, and GAC showing the observed (solid line) and synthetic (dashed line) waveforms. The correlated waveforms are indicated on the panels. (b) Particle motion diagrams for a time window of 8 seconds around the SPL phase on the data and synthetics for an event recorded at INK, and 10 seconds at LLLB and GAC showing

prograde elliptical motion diagnostic of the SPL phase. The red portions of the diagrams indicate beginning of the motion. (c) Marginal Posterior Probability Distributions (PPD) for example events recorded at seismic stations DRLN and GAC. More peaked distributions indicate more uniqueness among different models and fewer trade-offs among model parameters. Model parameter correlation matrices for the same events at DRLN and GAC. Each small square represents a model parameter on both axes. The correlations range between -1 and 1. Sparse colored squares off-diagonal indicate better constraints and lesser trade-offs in those parts of the models.....25

Figure 14: P- and S-wave velocity models (solid lines) for seismic stations in Canada. The P- and S-wave velocity models in FRB, MBC, and RES are from receiver function studies by Darbyshire (2003), and in GAC and INK are those from Cassidy (1995)....27

Tables

Table 1: Summary of crustal P- and S-wave velocities and depth of the Moho beneath Africa.....19

Table 2: Summary of crustal P- and S-wave velocities and depth of the Moho beneath China.....24

Table 3: Summary of crustal P- and S-wave velocities, depth of the Moho, and average crustal Poisson's ratio beneath Canada.....28

Acknowledgments

In this project we used data from the archives of the Incorporated Research Institutions for Seismology (IRIS). We made some figures in this report using the Generic Mapping Tools (GMT) software (Wessel and Smith, 1991). We acknowledge financial support for this project from Air Force Research Laboratory under Contract No. FA8718-04-C-0014 and the John A. and Katherine G. Jackson School of Geosciences and the Geology Foundation.

1. SUMMARY

In this project we developed a technique of waveform modeling, based on waveform fitting by synthetic seismograms, and demonstrated its application to determine the crust and upper mantle velocity structure beneath Africa, China, and Canada. In our method we generate the synthetic seismograms by the reflectivity method, and fit the observed waveforms by global optimization using a Very Fast Simulated Annealing. Our technique is complementary to the receiver function method in that it retains its advantages, uses a different part of the seismogram, is sensitive to both P- and S-wave velocities directly, and obtains helpful constraints in model parameters in the vicinity of the Moho. The method is particularly beneficial if the objective of using the velocity model is to determine the location and focal depths of small, regional seismic events, due to the characteristic feature of the shear-coupled PL phase, which this technique models wherever available, that it samples a broader area beneath the seismic station thereby representing a broad regional average. The technique also inverts for the P- and S-wave velocities independent of each other.

2. INTRODUCTION

Fundamental to the study of earthquakes is their accurate location. Among the location parameters, focal depth tends to be the most unconstrained. The primary reason for this is an inadequate knowledge of local and regional velocity structure. Seismologists use two broad categories of methods involving active and passive sources to determine the velocity structure of the Earth. Active source seismology, however, is cost-prohibitive, and in many cases not feasible. Therefore, passive source seismology which employs natural earthquakes as the source to generate seismic waves is mostly used to determine the velocity structure of the Earth. Nonetheless, passive source seismology can also be less effective if the region under consideration has relatively low rates of seismicity. Hence, rather than using common methods that analyze local and regional earthquakes, it is necessary to develop and employ techniques that use distant seismic sources to determine structure beneath such regions. In that category, two commonly used methods are receiver function analyses (e.g., Owens et al., 1984; Ammon et al., 1990), and surface wave dispersion studies (e.g., Julià et al., 2000; Pasyanos and Walter, 2002; Pasyanos, 2005). These methods are being used extensively in earthquake seismology to determine the one-dimensional shear wave velocity structure and depth of the crust–mantle boundary (Moho) beneath individual seismic stations using the reverberations of P-, and sometimes S-wave phases from earthquakes.

The objective of this project was to develop a third technique, based on waveform fitting by synthetic seismograms, and demonstrate its application to determine the crust and upper mantle structure of the Earth. In our technique we utilize the reflectivity method (Kennett, 1983) to compute the synthetic seismograms for an earthquake recorded at a particular seismic station and implement a global optimization algorithm using a Very Fast Simulated Annealing (VFSA) (Ingber, 1989; Sen and Stoffa, 1995) to invert for a one-dimensional velocity structure beneath that station. Our technique is complementary to the receiver function method in that it retains its advantages, uses a

different part of the seismogram, is sensitive to both P- and S-wave velocities directly, and obtains helpful constraints in model parameters in the vicinity of the Moho. The method is particularly beneficial if the objective of using the velocity model is to determine the location and focal depths of small, regional seismic events (Pulliam et al., 2002). The primary reason for this is the characteristic feature of the shear-coupled PL phase, which this technique models wherever available, that it samples a broader area beneath the seismic station thereby representing a broad regional average (Zhao et al., 1996; Zhao and Frohlich, 1996; Pulliam et al., 2002). Moreover, the technique also has the ability to invert for the P- and S-wave velocities independent of each other.

3. METHODOLOGY

3.1 Teleseismic Phases Modeled

In order to improve upon the sampling area beneath a seismic station, relative to receiver function inversions, when determining regional crustal velocity structure, and to obtain direct estimates of the P- and S-wave velocities, we modeled the S, Sp, SsPmP, and shear-coupled PL (SPL) phases in the waveforms of selected earthquakes. In Figures 1a and b we show typical paths of these waveforms through the crust and upper mantle from a teleseismic source. Correspondingly in Figure 1c we show these waveforms generated synthetically using PREM as the velocity model, and for a teleseismic source located at a focal depth of 600 km and recorded at an epicentral distance of 50°.

The traditional, direct S phase (path A-B in Figure 1a) is the initial, relatively sharp and higher amplitude, pulse-like arrival (Figure 1c) that indicates the beginning of a wave train with generally longer periods and normal dispersion (Pulliam and Sen, 2005). The particle motion of this phase is essentially rectilinear and all the three components of motion are in phase with each other.

Upon impinging on the crust-mantle boundary (Moho) from below, a portion of the S-wave converts to P-wave (path P-N-B in Figure 1a) which then travels through the crust to arrive at the seismic station as a precursor to the S-wave (Figure 1c). This phase is called Sp, has been used to model the crust in earlier studies (e.g., Jordan and Frazer, 1975; Owens and Zandt, 1997), and observed globally (Baag and Langston, 1986; Bock, 1988; Bock, 1991; Bock and Kind, 1991; Owens and Zandt, 1997). This waveform, however, samples a more localized region beneath the seismic station causing it to be less representative of a broader region and more similar to that of the P-coda (Pulliam and Sen, 2005).

The SsPmP phase arrives at the base of the crust as a S-wave, continues to travel through the crust upward as a S-wave, but then converts to a P-wave upon reflecting off the surface of the Earth, and finally bounces off the Moho once, to arrive at the seismographic station as a P-wave (Langston, 1996; Owens and Zandt, 1997; Pulliam and Sen, 2005) (path Q-M-N-B in Figure 1a). Langston (1996) demonstrated that this waveform is observed both at regional and teleseismic distances. He also noted however, that its propagation is dependent on the source depth and distance because it experiences a distance cross-over in the travel times causing it to arrive before the direct S-wave at regional distances, and after the S-wave at teleseismic distances, with equal or larger amplitude (Figure 1c), sometimes interfering with and thus distorting the direct S-pulse.

The dispersive wave train that sometimes follows S (Figure 1c) was named the “shear-coupled PL” (SPL) phase by Oliver (1961), who noted that it is analogous to the PL wave train and appears after S arrivals at regional and teleseismic distances. The particle motion of the SPL phase is prograde elliptical in nature and is confined to the vertical plane (Oliver, 1961). Based on observed group and phase velocities, Oliver (1961) also theorized that the SPL phase primarily is generated as a S-wave and then travels through the Earth’s mantle until it impinges upon the Moho, thereafter traveling as trapped P-waves and leaky SV-waves (Figure 1b). This hypothesis was later validated through presentation of computational methods for synthesizing SPL by Chander et al. (1968), Frazer (1977), and Baag and Langston (1985). SPL phases were also observed on regional and teleseismic seismograms of shallow and deep earthquakes recorded in Europe, North America, central Andes, and Asia (Zandt and Randall, 1985; Zhang and Langston, 1996; Zandt et al., 1996; Owens and Zandt, 1997; Swenson et al., 1999). The SPL phase samples a broader region beneath the seismographic station (Figure 1b) compared to the Sp phase, and its generation and propagation is affected by seismic velocity gradients, V_p/V_s ratios, impedance contrasts across the Moho, and thicknesses of the layers inside the Earth (Baag and Langston, 1985; Pulliam et al., 2002). With the exception of the direct S phase, all the other phases discussed above appear prominently only on the vertical and radial component seismograms at teleseismic distances (Figure 1c), due to their conversion from S- to P-type motion at some point in their paths.

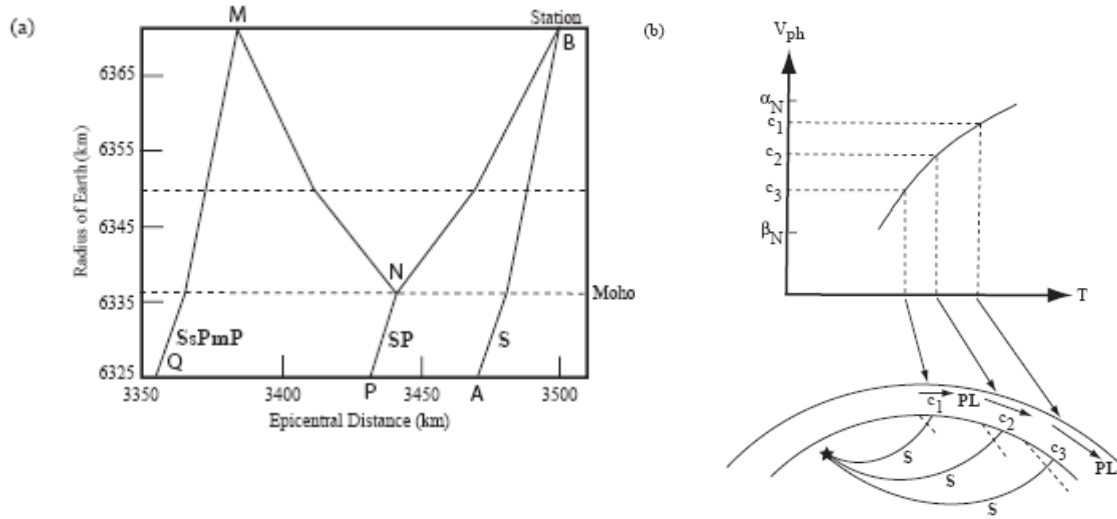


Figure 1: (a) Typical ray paths for S (path A-B), Sp (path P-N-B), and SsPmP (path Q-M-N-B) phases (Modified from Pulliam and Sen, 2005) (b) Propagation characteristics and excitation of shear-coupled PL waves with distance and corresponding phase velocity (V_{ph})-period (T) curve: α_N and β_N are the P and S wave velocities at the Moho, and c_1 , c_2 , and c_3 are the corresponding phase velocities as indicated (Modified from Baag and Langston, 1985).

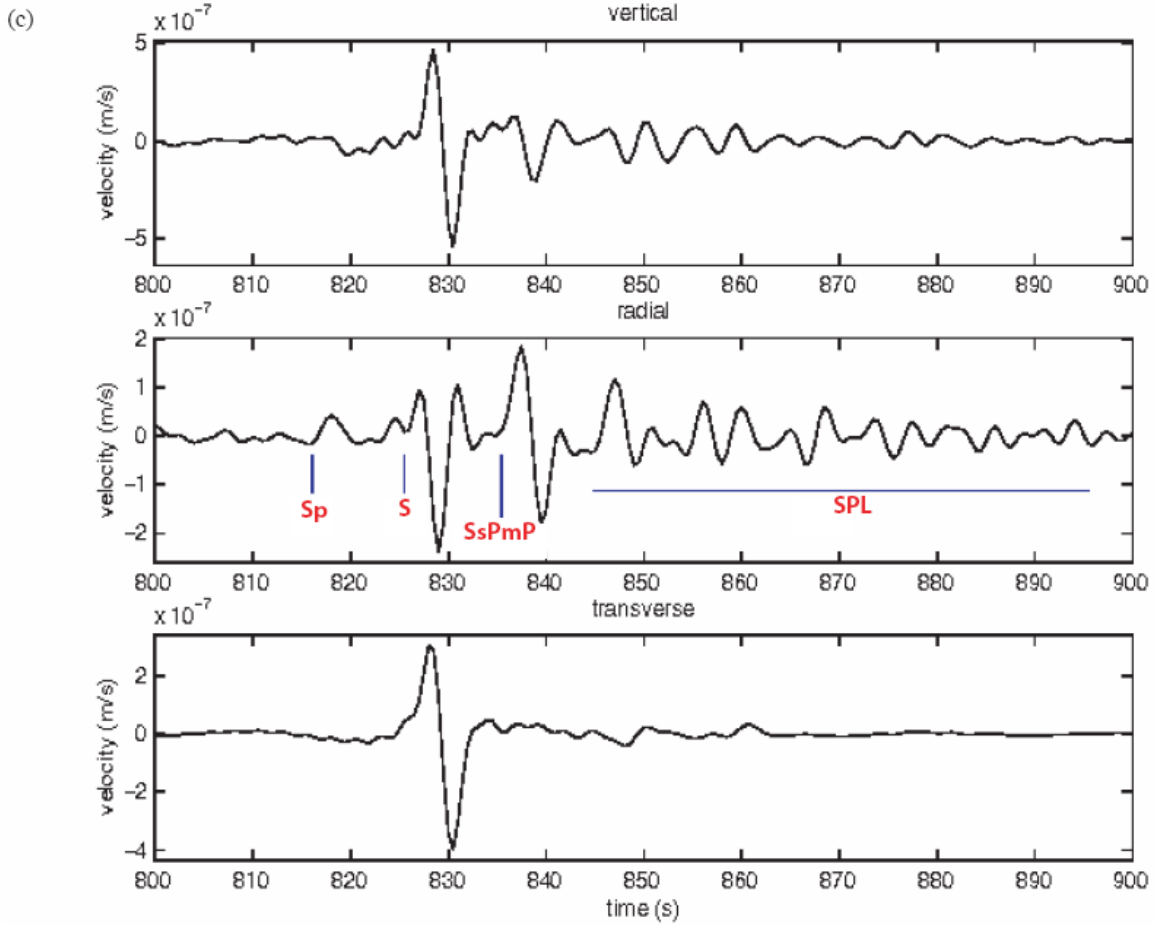


Figure 1: (c) Three-component synthetic seismograms generated by the parallelized reflectivity program used in this study, using PREM as the velocity model, and for a teleseismic source located at an epicentral distance of 50° and focal depth of 600 km. The onset of the S, Sp, SsPmP, and SPL phases are indicated on the radial component seismogram (Modified from Pulliam and Sen, 2005).

3.2 Waveform Modeling

Our waveform modeling technique combines a novel implementation of the reflectivity method (Kennett, 1983; Mallick and Frazer, 1987) with a global optimization algorithm (Sen and Stoffa, 1991; 1995). We compute the combined response of all layers of a candidate one-dimensional Earth model using the reflectivity method. The reflectivity calculation involves computation of reflectivity matrices for a stack of layers as a function of ray parameter and angular frequency, and produces all the phases possible for the specified stack of layers, source depth, and epicentral distance. The computations of the reflectivity responses for different ray parameters and frequencies are completely independent of each other. We use this independence to adapt the reflectivity program to parallel computer architectures, thereby decreasing the computation time nearly linearly with the number of processors used (Pulliam and Sen, 2004). We carry out message passing therein using the Message Passage Interface (MPI) Standard (Gropp and Lusk, 1995). We distribute the computation over the ray

parameters, and finally assemble the partial responses, and apply the inverse transformation from ray parameter to offset (a plane wave transformation) to generate synthetic seismograms at the required azimuths and distances.

Following the development of the forward problem, we perform an optimization procedure to determine for a given source-receiver pair, the model that produces synthetic waveforms which “best fit” the data. The criterion we use to determine the best fit is the combined cross-correlation between the vertical component of the data and synthetics, and radial component of the same, in a specified time window. In this application, we define the error as the negative of a correlation function (Sen and Stoffa, 1991) given by:

$$E(m) = -2[(\mathbf{d}_v \cdot \mathbf{s}_v)/\{|\mathbf{d}_v| + |\mathbf{s}_v|\} + (\mathbf{d}_r \cdot \mathbf{s}_r)/\{|\mathbf{d}_r| + |\mathbf{s}_r|\}]$$

where \mathbf{d}_v , \mathbf{d}_r , and \mathbf{s}_v , \mathbf{s}_r represent the vertical and radial components of the data and synthetics respectively, and $|\cdot|$ indicates the L2 norm.

Traditionally, when the forward problem is linear or there exists a weak non-linearity, derivative-based methods such as least squares are used to solve the inverse problem and estimate the model and its uncertainties (Tarantola, 1994; Sen and Stoffa, 1995). However, in the case of a non-linear problem such as is common in geophysics, these solution methods are generally not very successful. Therefore, in this method we employ a “global optimization algorithm” which is only weakly dependent on the choice of the initial model. In particular, we use a method called “Very Fast Simulated Annealing (VFSA)”, which is a variant of Simulated Annealing (SA) aimed at making the computations more efficient (Ingber, 1989; Sen and Stoffa, 1995).

Simulated Annealing (SA) is widely used to attain a global, rather than local, minimum while solving geophysical inverse problems (Sen and Stoffa, 1991; 1995 and references therein). The basic concepts of SA are derived from statistical mechanics, where an analogy is drawn between the optimization problem and a physical system. SA is analogous to the natural process of crystal annealing, in which a solid in a heat bath is initially heated by increasing the temperature such that all the particles are randomly distributed in a liquid phase, which then gradually cools. The optimization process involves simulating the evolution of the physical system as it cools and anneals into a state of minimum energy. At each temperature, the solid is allowed to reach thermal equilibrium where the probability of it being in that state is given by the Gibbs or Boltzmann probability density function (Sen and Stoffa, 1995). Very Fast Simulated Annealing (VFSA) is a variant of SA, developed in order to make it computationally more efficient. In particular, its salient features include the requirement of a temperature for each model parameter which can be different for different model parameters, and the use of a temperature in the acceptance criterion which may be different from the model parameter temperatures (Sen and Stoffa, 1995). To further illustrate the VFSA technique, we show a simplified flow-chart in Figure 2. The method starts with an initial model (\mathbf{m}^0) with an associated error or energy, $E(\mathbf{m}^0)$. It then draws a new model, \mathbf{m}^{new} , among a distribution of models from a temperature (T) dependent Cauchy-like distribution, $r(T)$, centered on the current model (Figure 2). The associated error or energy, $E(\mathbf{m}^{\text{new}})$, is then computed and compared with $E(\mathbf{m}^0)$ (Figure 2). If the change in energy (δE) is less than or equal to zero, the new model is accepted and replaces the initial model. However, if the above condition is not satisfied, \mathbf{m}^{new} is accepted with a probability of $[e^{\delta E/T}]$ (Figure 2). This rule of probabilistic acceptance in SA allows it to escape a local minimum. We

repeat the processes of model generation and acceptance a large number of times with the annealing temperature gradually decreasing according to a pre-defined cooling schedule (Figure 2). VFSA is more efficient than the traditional SA because it allows for larger sampling of the model space during the early stages of the waveform fitting, and much narrower sampling in the model space as the procedure converges and the temperature decreases, while still allowing the search to escape from the local minima. Additionally, the ability to perform different perturbations for different model parameters allows for individual control of each parameter and the incorporation of *a priori* information (Sen and Stoffa, 1995).

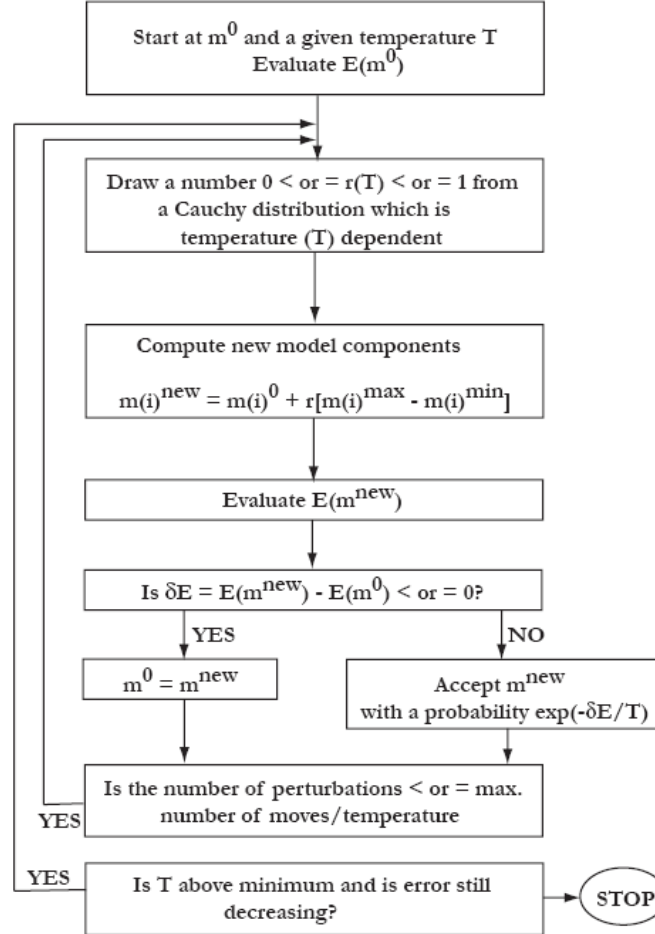


Figure 2: Flow-chart elaborating the Very Fast Simulated Annealing (VFSA) algorithm used in this study for the waveform inversion by global optimization (Modified from Sen and Stoffa, 1995). $E(m^0)$ – error function for the initial model m^0 . $E(m^{\text{new}})$ – error function for the new model m^{new} , T = temperature, $r(T)$ – temperature dependent Cauchy-like distribution.

3.3 Estimation of Uncertainties

It is widely known that solutions to geophysical inverse problems are often non-unique. That is, their error functions either have broad minima or are multi-valued,

indicating that models that are slightly different from the best-fitting model satisfy the data nearly as well, in the first case, or that one or more very different models also satisfy the data, in the second case. It is therefore necessary to explore the model space and thus identify the range of models that fit the data, and perhaps to identify characteristics of the models that are required by the data, rather than which simply are allowed by the data. VFSA conducts such a search efficiently, and the products of multiple such searches enable us to evaluate the uncertainty in a single, best-fitting solution. This evaluation is particularly necessary in seismic waveform modeling because more than one model can often explain the observed data equally well and trade-offs between different model parameters are common (Pulliam and Sen, 2005). The waveform modeling method we developed incorporates important statistical tools that allow the user to evaluate the uniqueness, and physical feasibility of the resulting model. The most useful of these tools in evaluating the results' reliability are the Posterior Probability Density (PPD) function, and the parameter correlation matrix. To estimate these statistical parameters we cast the inverse problem in a Bayesian framework (e.g., Tarantola, 1994; Sen and Stoffa, 1995), and employ "importance sampling" based on a Gibbs' sampler (GS) (Sen and Stoffa, 1995; Pulliam and Sen, 2005). The goal of "importance sampling" is to concentrate sample points in the regions that are the most "significant", in some sense (perhaps, for example, where the error function is rapidly varying, or many acceptable solutions lie). Because this concentration is achieved using a Gibbs' probability distribution, it has been named the "Gibbs' sampler" (Sen and Stoffa, 1995). The Posterior Probability Density (PPD) function $[\sigma(\mathbf{m}|\mathbf{d}_{obs})]$ is defined as a product of a likelihood function $[e^{-E(\mathbf{m})}]$, and prior probability density function, $p(\mathbf{m})$. The prior probability density function $p(\mathbf{m})$, describes the available information on the model without the knowledge of the data and defines the probability of the model \mathbf{m} independent of the data. In our applications, we use a uniform prior within a minimum and maximum bound for each model parameter. The likelihood function defines the data misfit and its choice depends on the distribution of error in the data (Sen and Stoffa, 1995 and references therein). Sen and Stoffa (1996) examined several different approaches to sampling models from the PPD and concluded that a multiple-VFSA based approach, though theoretically approximate, is the most efficient. In a multiple-VFSA approach we make several VFSA runs (20 in this study) with different random starting models and use all the models sampled along to characterize uncertainty in the model. We use all these sampled models to compute approximate marginal PPD and posterior correlation matrices to characterize uncertainties in the derived results. The posterior correlation matrix measures the relative trade-off between individual model parameters and is computed by normalizing the covariance between two model parameters (Sen and Stoffa, 1996). Computationally, the correlation between i^{th} and j^{th} model parameters is given by their covariances divided by the square root of the product of the covariances of each parameter with itself. In a later section during discussion of the application of the technique to seismological data recorded in Africa, we provide descriptions of interpretations of the resulting computations of the PPD and correlation matrix.

4. RESULTS – APPLICATION OF THE METHOD

We applied our modeling method described above to data from large-magnitude, deep-focus earthquakes recorded teleseismically during 1976 – 2005 at permanent broadband seismic stations spanning the continent of Africa, China and Canada. The focal depths of these earthquakes range between 200 km and 600 km, and their magnitudes lie between 5.5 and 7.0. Since the goal is to also model the SPL phase that is generated close to the seismic station (within an area of $\sim 100 \text{ km} \times 100 \text{ km}$) (Frazer, 1977), we chose such a focal depth range to eliminate the SPL phase generated at the earthquake source. Epicentral distances from the seismic stations of the selected earthquakes are between 30° and 80° so as to avoid possible incorporation of phases that interacted with the Earth's core. Initially, we filtered the raw data obtained from the global database for the selected events, using a six-pole Butterworth bandpass filter with corner frequencies of 0.005 and 0.25 Hertz respectively. We then decimated the data such that the sample interval is 0.5 seconds. The data window we analyzed includes 30 seconds prior to the arrival of the direct S phase and 180 seconds following it. The choice of the beginning time for our data window follows from a study by Jordan and Frazer (1975) who showed that for a deep focus event ($\sim 600 \text{ km}$) of intermediate magnitude (~ 6.1), at teleseismic distances, the Sp phase resulting from a single conversion at the Moho ($\sim 35 \text{ km}$ - 40 km), precedes the S phase by about 5-6 seconds. Since the events we modeled in these applications also lie in that category, and the only phase arriving before the S phase that we model is the Sp, we do not expect to observe any Moho-converted Sp phase before ~ 15 seconds from the S phase. Therefore, the start time of our data window (30 seconds before the S arrival) provides ample lead time for us to never miss the observation of the Sp phase if any. For each station, the initial model we chose is one obtained from a previous published study, wherever available, or Preliminary Reference Earth Model (PREM) (Dziewonski and Anderson, 1981) where an earlier study has not been published. We also experimented with an initial model consisting of crustal layers of equal thickness and increasing velocities, superimposed on PREM. However, the final models obtained using our method were similar within one standard error, thereby emphasizing minimal dependence of our method on the starting model. For use in reflectivity computations, we also incorporate the source mechanism of each earthquake from the Global CMT catalog, and use a Gaussian source-time function. Following similar forward calculations for each source – receiver pair, we carried out the waveform fitting procedure for each using 200 iterations. Prior to our choice of the number of iterations, we experimented with 200, 400, 600, and 800 iterations, and have consistently observed that after ~ 165 iterations the error reaches an optimal value and does not change with subsequent iterations. This feature is a diagnosis in our method to confirm that the process has converged. Therefore, we chose 200 iterations as a threshold for all our computations. Additionally, earlier studies (Sen and Stoffa, 1995 and references therein) have shown that Very Fast Simulated Annealing (VFSA) typically converges significantly faster than other methods in the category, hence the name. Based on examples documented by Sen and Stoffa (1995), we chose an initial temperature of 10^{-3} units at the start of our waveform fitting process for each model parameter and allowed it to cool down to 10^{-10} units throughout the process. In our method, we allowed each model parameter (velocity of the P-wave, V_p , velocity of the S-wave, V_s , thickness of the

layer, and density) to vary within $\pm 10\%$ of initial values. We conducted trial runs with the model parameters varied within $\pm 10\%$, $\pm 15\%$, $\pm 20\%$, and $\pm 30\%$. Our results produced similar final models that were within one standard error. Additionally, a significant variation in model parameters is not realistic given the tectonic and geologic setting of the regions. Therefore, to maintain reasonable computational time and to allow variations that are more realistic, we varied the model parameters $\pm 10\%$.

Below, we report results of waveform fitting for selected teleseismic earthquakes recorded in Africa, China and Canada. Work is currently ongoing on the data from China and Canada. The detailed study of crust and upper mantle velocity structure beneath Africa using our method is presented in Gangopadhyay et al. (2007), therefore herein we only discuss important results from that study. For the seismic stations that recorded better quality data overall, we show the waveform correlations for events recorded at that station, and also describe the interpretations of the uncertainty computations as an example. A comment on amplitude matches: The most successful match between synthetics and data would be one in which the synthetic waveform matched the data exactly – wiggle for wiggle. This is unrealistic for several reasons, including the fact that models used to compute synthetics are layered, isotropic, limited to ten to sixteen layers, and have fixed attenuation (Q) values. Further, the source time function is assumed to be Gaussian and its focal mechanism is assumed to be correctly represented by Harvard’s CMT solution. To minimize complexities in the source time function we avoid very large earthquakes. Given the uncertainties in model Q and focal mechanisms, which will largely control relative amplitudes of various phases, we focus our fitting criteria on matching each phase’s arrival time, polarity, and pulse character. Fitting the amplitude of each phase, while desirable, is deemed to be of lesser importance.

4.1 Africa

We applied our modeling method to data recorded at twelve permanent broadband seismic stations spanning the continent of Africa (Figure 3). A total of seventeen earthquakes were used in this study selected from the global catalog of Centroid Moment Tensors (CMT) (1976 – 2004). The region encompassing north and west Africa includes the seismic stations of TAM, DBIC, MBO, and MDT (Figure 3). Among these stations, TAM recorded data of better quality; examples of the waveform fits for three events recorded at TAM are shown in Figure 4a. We observe S, Sp, and SsPmP phases consistently on all these event seismograms and they correlate well with the synthetics generated by the optimization technique (Figure 4a). On event 3, we also observe a prominent SPL phase and the synthetics match it well (Figure 4a). Particle motion diagrams for the corresponding time window on both data and synthetics confirm this observation (Figure 4b). We observe prograde elliptical particle motion, which is diagnostic of the SPL phase, on both diagrams (Figure 4b). Except for event 3, none of the others have any signature of the SPL phase, as confirmed by particle motion diagrams for corresponding time windows. This observation – that one source-receiver pair would show SPL while other, similar paths would not – is unexpected and we cannot explain it.

Based on the waveform-fitting results for all six events recorded at TAM, we generate P- and S-wave velocity models up to a depth of 100 km (Figure 4c). We observe some variability in the models (Figure 4c), and hence compute the uncertainties for each

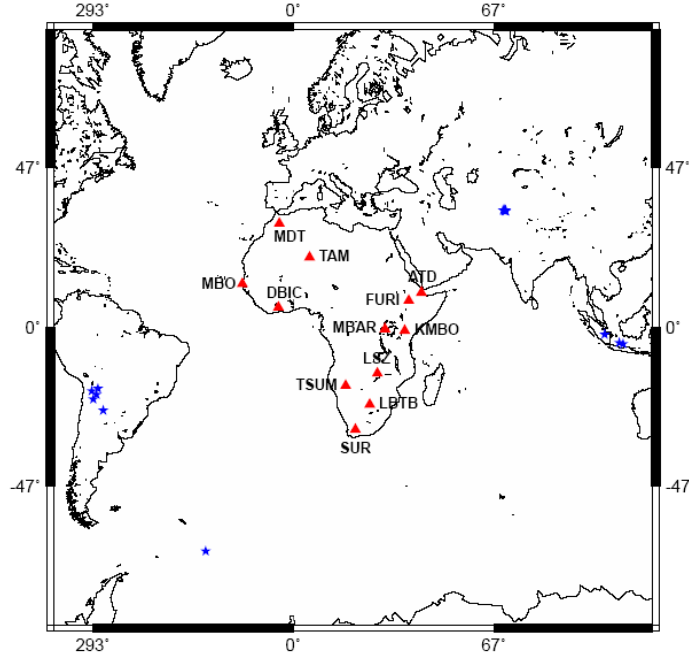


Figure 3: Map showing locations of the earthquakes used in this study (blue stars) and the permanent broadband seismic stations in the African continent (red triangles) that have recorded these earthquakes. The respective station codes are shown adjacent to each seismic station.

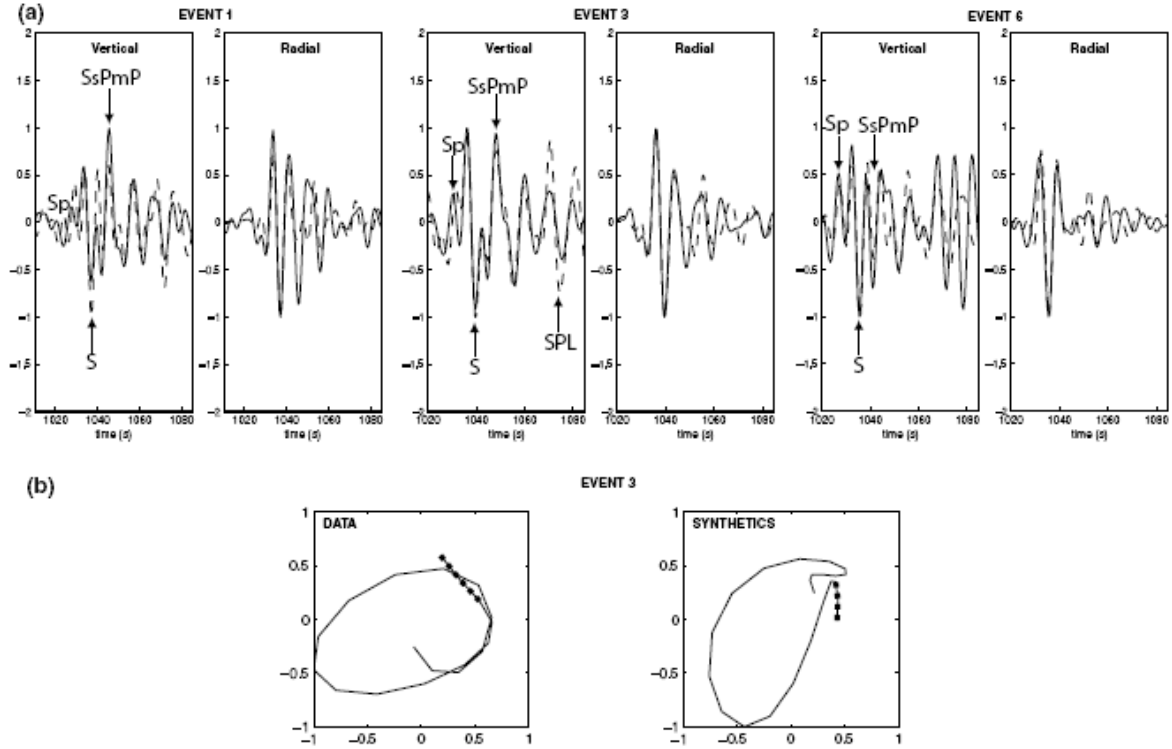


Figure 4: (a) Vertical and radial component seismograms for three events recorded at TAM showing the observed (solid line) and synthetic (dashed line) waveforms. The correlated waveforms are indicated on the panels. (b) Particle motion diagrams for a 10-s

time window around the SPL arrivals for event 3 showing the diagnostic prograde elliptical motion of the SPL phase. The dotted portions of the diagrams indicate the beginning of the motion.

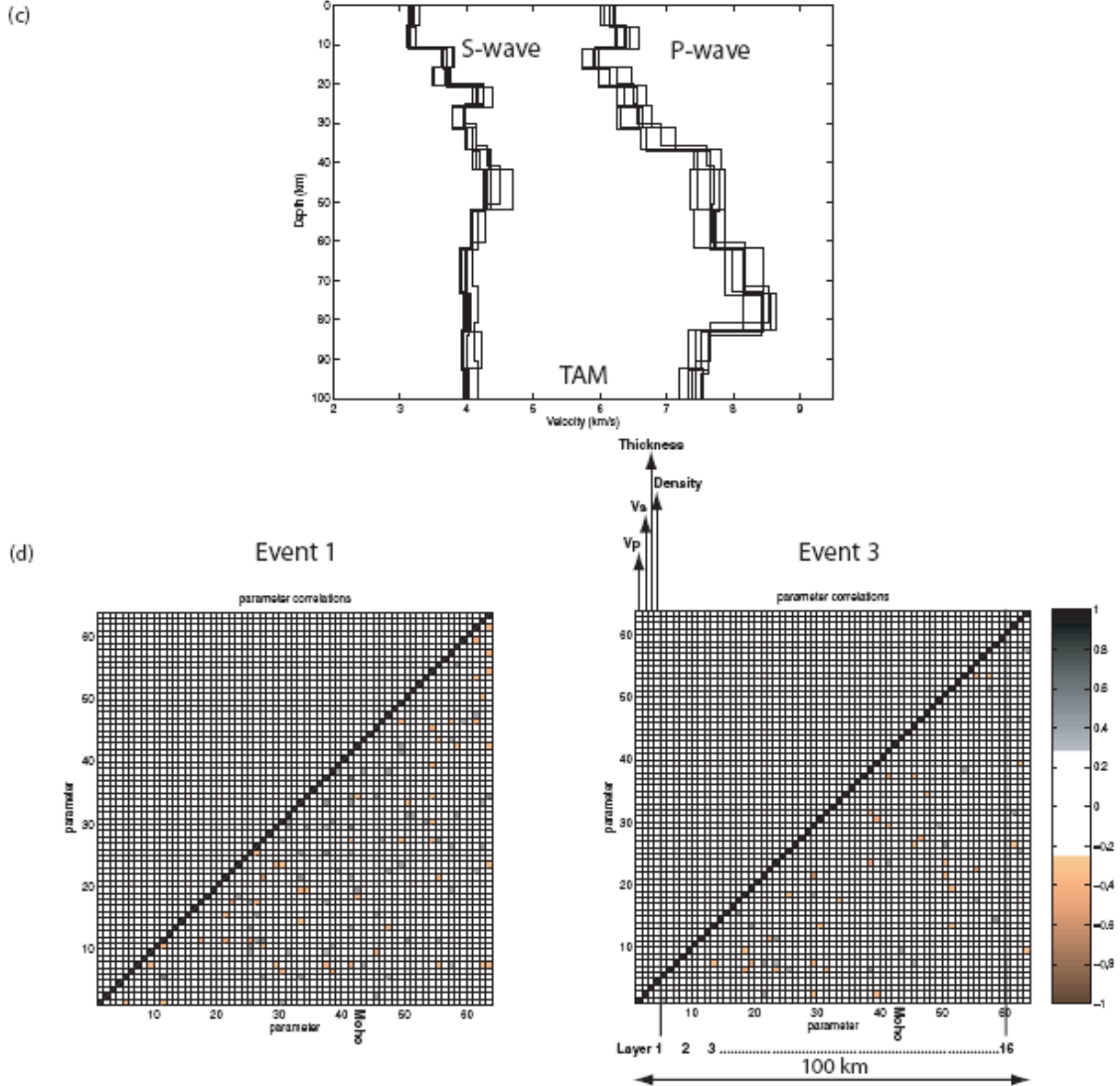


Figure 4: (c) P- and S-wave velocity models up to 100 km for station TAM from the inversion results for individual events recorded at TAM. (d) Model parameter correlation matrices for events 1 (left-hand panel) and 3 (right-hand panel) recorded at TAM. Each small square represents a model parameter (V_p , V_s , Thickness of layer, and Density) on both the horizontal and vertical axes. The correlations range between -1 and 1. Sparse colored squares off-diagonal in the lower crust-upper mantle in event 3 (right-hand panel) compared to that in event 1 (left-hand panel) indicate better resolution and confidence (less trade-off) in this region.

model using the statistical tools described earlier to choose the “best” model. In Figure 4d, we show examples of parameter correlation matrices computed from the modeling results of events 1 and 3. Each small square along an axis of the parameter correlation

matrix, either horizontally or vertically, represents a model parameter (Figure 4d). Since every model layer consists of four independent model parameters (V_p , V_s , thickness, and density), four small squares combined together represent a model layer on both axes (Figure 4d). Correlation values range between -1 and 1 and are symmetric about the diagonal of the matrix, hence, for clarity, we show only values below the diagonal (Figure 4d). Values along the diagonal are ones, simply indicating that each parameter is perfectly correlated with itself. Off-diagonal colored squares indicate significant cross-correlation (trade-offs) between corresponding model parameters. In the parameter correlation matrices for both events (Figure 4d), layers comprising the upper crust have greater independence, as indicated by the sparse distribution of off-diagonal cross-correlations whose absolute values are greater than ± 0.5 (colored squares). Also, for both events, the level of tradeoffs among model parameters in these shallow layers is similar (Figure 4d). For event 1, however, the layers comprising the lower crust and upper mantle have larger off-diagonal cross-correlations, indicating significant tradeoffs (Figure 4d). On the contrary, for event 3, even the lower crustal and upper mantle layers appear better constrained (Figure 4d). Intriguingly, the SPL phase is also observed in the seismogram of event 3 but not in that of event 1 (Figure 4a). This observation attests to the fact that, if SPL is present in the seismogram and is well modeled, we are able to better constrain the structure of the lower crust and upper mantle. This result, which is expected, due to the sensitivity of SPL to those parts of the model (Figure 1b), drives our decision to generate velocity models down to the Moho for seismic stations at which SPL is not observed.

We observed and successfully fit S and SP phases in seismograms recorded at DBIC and at MBO. The SsPmP phase appears on the vertical-component seismograms of an event at DBIC and one at MBO but is absent on their radial-component seismograms. We do not observe the SPL phase in seismograms recorded at DBIC but do so in the seismograms at MBO. The SPL phase is prominent on both vertical and radial component seismograms of the event recorded at MBO, which we confirm with particle motion diagrams that show prograde elliptical motion for the corresponding time window. At MDT, within the time-window expected to contain the phases analyzed in this study, we were unable to clearly identify them and they appear to be contaminated by interfering arrivals, and hence are also not well-correlated with the synthetics generated by the waveform modeling process. Station MDT is located near the Atlas Mountains in Morocco, and so may be underlain by complicated three-dimensional structure, which the waveform modeling program used in this study is unable to model accurately. The lack of proper correlation between the synthetic seismograms and the data at MDT is likely a consequence of this limitation.

East Africa contains the permanent broadband seismic stations ATD, FURI, KMBO, and MBAR (Figure 3). However, these stations are situated within and on the flanks of the active East African rift system and therefore waves recorded at these stations sample the complicated three-dimensional, anisotropic structure beneath the rift (Ayele et al., 2004; Dugda and Nyblade, 2006). The three-dimensional structure is manifested in the seismograms as numerous, possibly scattered, refracted, or split, phase arrivals with strong interference amongst themselves. Anisotropy inferred from shear-wave splitting studies has also been reported for stations ATD, FURI, and KMBO by Ayele et al. (2004). As we note earlier, the waveform inversion method we use in this

study is capable of estimating azimuthally dependent one-dimensional (although azimuthally dependent) structure only, hence waveforms for events recorded at these stations are not precisely correlated in some cases. On both the vertical and radial component seismograms of most events at ATD, FURI, KMBO, and MBAR, we observe S and SsPmP phases. On the other hand, except at MBAR, we observe the SP phase only on the vertical component for these events. Only at FURI, for event 12, and MBAR, for event 15, did we see SPL phase in the seismograms.

Seismic stations TSUM, LSZ, LBTB, and SUR are located in southern Africa (Figure 3). However, for the lone event recorded at SUR, we are able to identify only the direct S phase, and thus we do not attempt to generate P- and S-wave velocity models for SUR. We observe and successfully fit S, Sp, and SsPmP phases on events 13 and 14 recorded at TSUM, event 9 recorded at LSZ, and event 11 at LBTB. But, except for event 13 at TSUM, we are able to identify the Sp phase on both the vertical and radial component seismograms at TSUM, LSZ, and LBTB. Similarly, the SsPmP phase is only identifiable on the vertical component seismogram for events 14 and 9 recorded at TSUM and LSZ respectively. It is, however, absent on the seismograms for event 13 at TSUM. We do not observe the SPL phase in the seismograms of any event recorded at these stations.

For each seismic station in the three broad regions of the African continent, based on the waveform correlations described earlier, we generate azimuthally dependent P- and S-wave velocity models beneath the station. At the seismic stations where the SPL phase is not observed and modeled, we only generate velocity models up to the crust–mantle boundary (Moho), since the body-wave phases Sp, SsPmP, and S do not constrain models below the Moho. Where SPL is observed we generate the velocity models up to an arbitrarily chosen depth of 100 km. Wherever available, we compare our velocity models with those obtained from earlier studies for the stations.

Figures 5a–d shows the obtained P- and S-wave velocity models for the north and west African stations of TAM, DBIC, MBO, and MDT. The estimates of crustal thickness beneath these stations range between 36 km and 42 km (Figures 5a–d), comparable to regional estimates of 34 km to 40 km by Pasyanos et al. (2004). We also note that the crust is slightly more thick in west Africa beneath seismic stations DBIC and MBO (~41–42 km) (Figures 5b and 5c), compared to the seismic stations TAM and MDT in north Africa (~36 km–38 km) (Figures 5a and 5d). A similar observation was also made earlier by Pasyanos and Walter (2002) using surface wave dispersion tomography, and by Marone et al. (2003) using joint inversion of local, regional, and teleseismic data. Except for TAM, the crust below all the stations appears to be fairly simple in structure (Figures 4a–d) (Sandvol et al., 1998), suggesting that it is minimally affected by large-scale tectonic processes. However, a middle to lower crustal low-velocity zone obtained beneath all the seismic stations in the region (Figures 5a–d), indicate possible local tectonic influences. Our estimate of crustal thickness beneath TAM (~36 km) is similar to that obtained from receiver function studies by Sandvol et al. (1998) (38 ± 2 km) (Figure 5a), from Rayleigh wave group velocity dispersion studies by Hazler et al. (2001) (43 ± 5 km), and from surface-wave dispersion tomography by Pasyanos and Walter (2002) (~40 km). TAM is close to the location of the Hoggar hot spot but, as noted by Sandvol et al. (1998), the crustal thickness indicates that a mantle plume has not significantly altered the crust here. However, in contrast to the model of

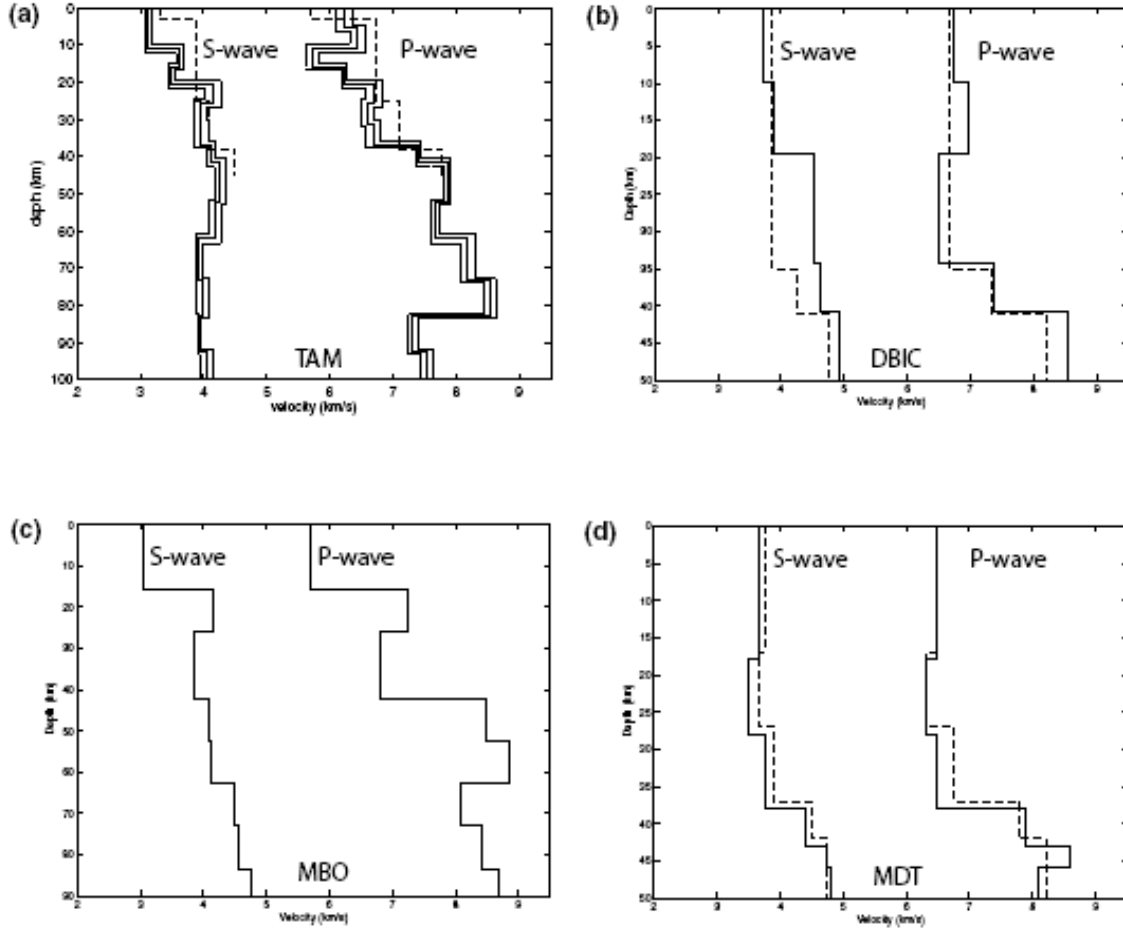


Figure 5: Preferred P- and S-wave velocity models for (a) TAM (b) DBIC (c) MBO and (d) MDT. The P- and S-wave velocity models (broken lines) in (a), (b), and (d) are from receiver function studies by Sandvol et al. (1998). The dotted lines in (a) show the P- and S-wave velocity model for TAM within \pm two standard errors.

Sandvol et al. (1998), the crustal P- and S-wave velocities we obtain in this study at TAM, are both slightly lower (Figure 5a). These velocities at TAM range between 6.25 km/s–6.8 km/s, and 3.1 km/s–3.9 km/s, respectively (Figure 5a). Upper mantle P-wave velocities exhibit a gradational increase with depth below the Moho, whereas the S-wave velocities are nearly constant (4 km/s–4.2 km/s) within that range of depths (Figure 5a). Furthermore, we also obtain an anomalous low-velocity zone of ~5 km thickness at the base of the upper crust (Figure 5a) that appears to be well constrained based on the uncertainty estimates described earlier (Figure 4d). However, we are unable to confirm the existence of this layer from any other independent studies. At the west African coastal station DBIC, we obtain a Moho depth of ~41 km which is similar to that obtained by Sandvol et al. (1998) ($\sim 40 \pm 2.3$ km) (Figure 5b). P-wave velocities range between 6.7 km/s–7 km/s in the upper crust, and 6.5 km/s–7.3 km/s in the lower crust (Figure 5b). On the contrary, S-wave velocities show a gradational increase in the crust with depth from 3.7 km/s–4.7 km/s (Figure 5b). Anomalous V_p/V_s ratios are thus caused by a low P-wave velocity zone of ~15 km thickness in the lower crust. However, due to the trade-offs

between the model parameters in this depth range, we conclude that this anomaly is not well-constrained. Beneath MBO, any prior P- and/or S-wave velocity models are absent. Sandvol et al. (1998) had analyzed seismic data recorded at MBO but the anomalous data did not allow them to estimate a velocity model. Thus, the velocity model for MBO that we obtain from this study, is to our knowledge, the first estimate of its kind. We obtain a crustal thickness of ~ 42 km (Figure 5c), which is similar to that found underneath other stations in the region. A regional crustal thickness of 43 ± 5 km obtained from Rayleigh wave group velocity dispersion studies (Hazler et al., 2001) correlates well with the results of this study at MBO. The P- and S-wave velocities at MBO in the crust range between 5.6 km/s–7.2 km/s, and 3.1 km/s–4.1 km/s, respectively (Figure 5c). We also observe an anomalous lower crustal, approximately 15 km-thick zone of relatively low P- and S-wave velocities (6.8 km/s and 3.8 km/s) beneath MBO (Figure 5c). Our P- and S-wave velocity models beneath MDT predict a Moho depth of ~ 38 km (Figure 5d). Surprisingly, even with the poor waveform fit by synthetics to the event recorded at MDT, this result is consistent with the estimates obtained by Sandvol et al. (1998) (36 ± 1.3 km). As also noted by Sandvol et al. (1998) and Pasyanos and Walter (2002), the slightly shallower Moho at MDT, compared to that at DBIC and MBO, indicates that in spite of its proximity to the Atlas Mountains, there is no crustal thickening associated with them, and a significant root is absent beneath the mountains. Sandvol et al. (1998) concluded that this may be a possible outcome of the fact that there existed a failed rift earlier which was subsequently inverted. In this study, beneath MDT, we obtain average P- and S-wave velocities in the crust of ~ 6.4 km/s and 3.7 km/s, respectively, except in a low-velocity zone of ~ 10 km thickness in the lower crust where these are 6.2 km/s and 3.4 km/s, respectively (Figure 5d). A similar zone has also been postulated by the earlier velocity model obtained from receiver function studies (Sandvol et al., 1998). However, because of poor waveform fits at MDT in this study, we are unable to postulate the existence of this zone.

For east Africa, we generate P- and S-wave velocity models beneath seismic stations ATD, FURI, KMBO, and MBAR, which are shown in Figures 6a-d. Located within and on the flanks of the East African Rift System, which is relatively well studied, these stations are situated in active tectonic domains. Except beneath ATD (Figure 6a), where the crust is significantly thin compared to the other stations in the region (Figures 6d-f), the Moho is generally between ~ 38 km–41 km deep. The estimate of crustal thickness beneath ATD, however, is the subject of an active debate. Using a grid search method to model receiver functions for eleven earthquakes recorded at ATD, Sandvol et al. (1998) obtained a crustal thickness of ~ 10 km (Figure 6a). But, Dugda and Nyblade (2006) used H- κ analysis of receiver functions and predicted a crustal thickness of $\sim 23 \pm 1.5$ km beneath ATD, consistent with earlier results from inversion of gravity data for the general area by Tiberi et al. (2005). In this study, our velocity model beneath ATD shows comparable velocity discontinuities at ~ 10 km and ~ 21 km depths (Figure 6a), suggesting that either of these depths could be interpreted as the Moho. However, the layer at 10 km depth appears to be poorly constrained compared to the layer at ~ 21 km depth, as evidenced from the PPD (Figure 6b) and the parameter correlation matrix (Figure 6c) computations. Therefore, we prefer a crustal thickness of ~ 21 km. Irrespective of the debate on the crustal thickness at ATD, the crust beneath it is significantly thinner than the crust beneath other seismic stations in east Africa (Figures 6d–f). Located within the

Afar depression, close to the coast of the Red sea on the eastern edge of the African continent, such a thin crust is expected at ATD because of highly stretched continental crust (Sandvol et al., 1998).

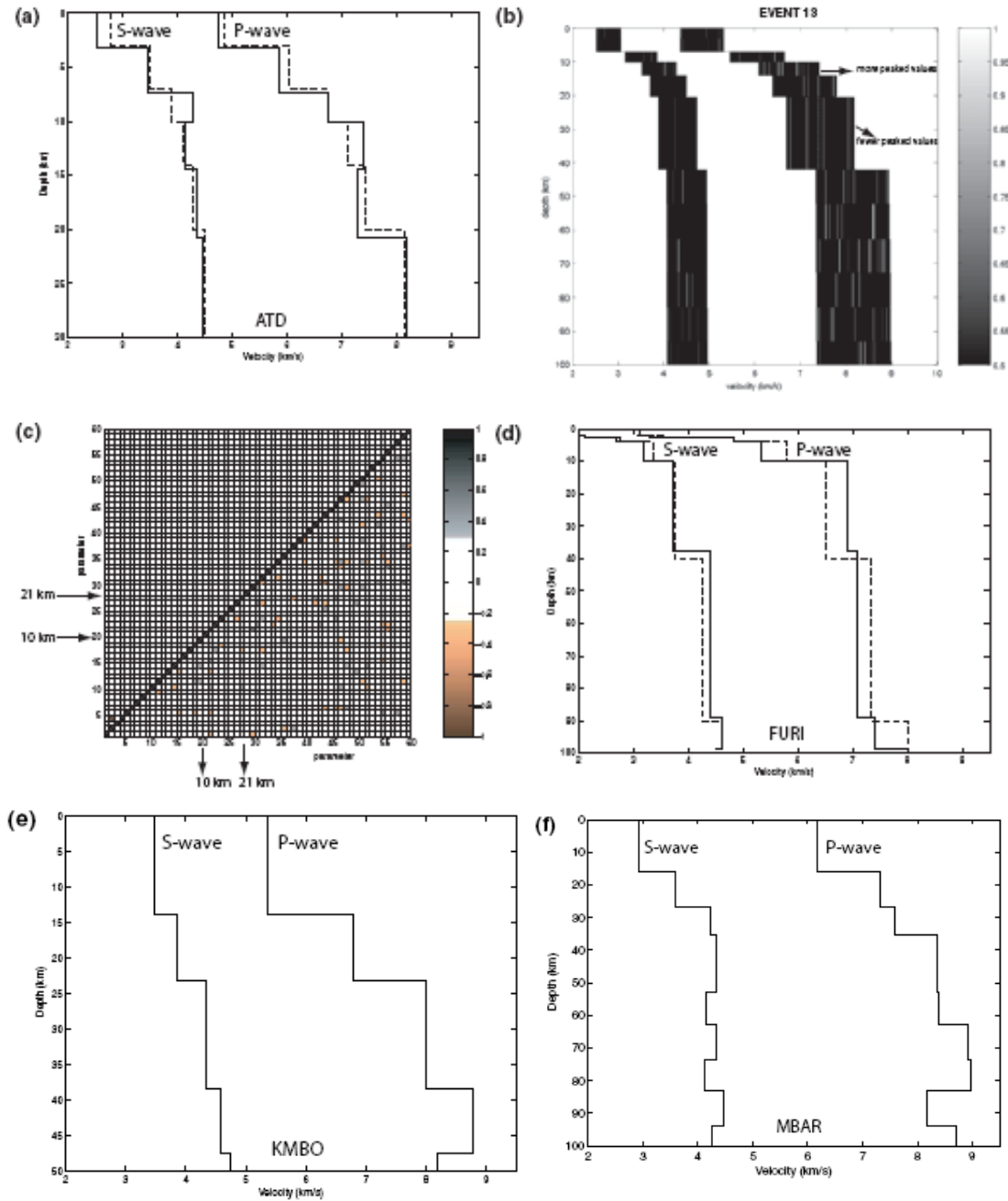


Figure 6: (a) Obtained velocity model from this study (solid line) up to 30 km for station ATD and available velocity model from Sandvol et al. (1998) (broken line). Posterior Probability Distribution (b) and parameter correlation matrix (c) for event 13 recorded at ATD showing the tradeoffs between different model parameters in different layers. (d) Obtained velocity model from this study (solid line) up to 100 km for station FURI and available velocity model from Ayele et al. (2004) (broken line). Preferred P- and S-wave

velocity models for (e) KMBO up to a depth of 50 km, and (f) MBAR up to a depth of 100 km.

The P- and S-wave velocities in the crust at ATD range between 4.7 km/s–7.2 km/s, and 2.5 km/s–4.3 km/s, respectively (Figure 6a). Crustal P-wave velocities below about 5 km depth are relatively high and, as noted by Dugda and Nyblade (2006), could indicate a highly mafic composition caused by igneous rock emplacement during the syn-rift stage. Figure 6d shows the preferred P- and S-wave velocity models beneath FURI which is situated in the northern part of the western Ethiopian plateau. We obtain an estimate of crustal thickness beneath FURI of ~39 km, which is similar to that obtained using receiver function analyses by Ayele et al. (2004) (~40 km), and Dugda et al. (2005) (~44 km). The ~40 km thick crust beneath FURI, which is located close to the border of the western Ethiopian plateau and the Afar depression, is also consistent with previous refraction studies of as reported by Ayele et al. (2004). Crustal P- and S-wave velocities below ~5 km depth at FURI range between 5.3 km/s–6.8 km/s, and 3.2 km/s–3.6 km/s, respectively (Figure 6d). In addition, beneath FURI, our results also predict an ~50 km thick layer immediately below the Moho in the upper mantle that has P- and S- wave velocities of ~7.1 km/s and ~4.3 km/s, respectively, which are anomalously slow (Figure 6d). A similar layer with P- and S- wave velocities of ~7.4 km/s and ~4.2 km/s, respectively, was also obtained by Ayele et al. (2004) (Figure 6d). As noted by Ayele et al. (2004), this anomalously slow layer possibly indicates altered lithospheric material, and supports an earlier result from Rayleigh wave dispersion of an approximately 100 km thick lithosphere beneath FURI. Station KMBO is located in Kenya, close to the southern end of the eastern branch of the East African Rift System, but outside its edge. Beneath KMBO our estimate of the crustal thickness is ~38 km (Figure 6e). This estimate is similar to that obtained using receiver function analysis by Dugda et al. (2005) (~41 km). Crustal P- and S-wave velocities show a gradational increase with depth and range between 5.4 km/s–8 km/s, and 3.5 km/s–4.5 km/s, respectively (Figure 6e). The velocity structure beneath KMBO appears to be fairly simple. Although it has relatively high P-wave velocities in the lower crust (Figure 6e), it is otherwise typical of cratonic regions. Seismic station MBAR is located between the western boundary of the Tanzania craton and the western branch of the East African Rift System. Due to poor correlation of some of the observed phases with synthetics, and the availability of only one event, the resulting velocity model from our study beneath MBAR is poorly constrained. Nevertheless, our estimate of crustal thickness beneath MBAR, to our knowledge the first of its kind, is ~41 km (Figure 6f), and is consistent with that obtained from other stations in the region. Crustal P- and S-wave velocities at MBAR range between 5.3 km/s–7.7 km/s, and 3.2 km/s–3.8 km/s, respectively (Figure 6f). Our model also predicts a low P-wave velocity (~7.2 km/s) layer beneath the crust (Figure 6f). Such a layer promotes the generation of the SPL phase near the station, which we observe in both data and synthetics for the event recorded at MBAR. Therefore, in spite of the poorly constrained model obtained in this study, we cannot rule out the possibility of its existence.

Southern Africa is another of the better studied regions in Africa. To add to the existing knowledge base, our study generated P- and S-wave velocity models beneath the seismic stations TSUM, LSZ, and LBTB (Figures 7a-c). Although we analyzed seismic data recorded at SUR, due to the lack of identifiable phases, we do not generate P- and S-wave velocity models for the station. Similar to most of the results in north and west

Africa, our results for southern Africa are representative of stable shield regions. However, in general, we obtain slightly higher crustal thicknesses ranging between ~42 km and 46 km (Figures 7a-c). We also predict crustal low velocity zones as discussed later in our models beneath two of the three stations in southern Africa. Beneath TSUM, to our knowledge, no prior velocity model exists. Thus, the velocity model obtained from our study at TSUM is the first of its kind. We obtained a crustal thickness beneath TSUM of ~42 km (Figure 7a). The velocities of P- and S-waves in the crust range between 6.3 km/s–7.3 km/s, and 3.2 km/s–4 km/s, respectively (Figure 7a). These results are similar to those obtained for the seismic stations in north and west Africa and are therefore representative of stable shield regions. We do not obtain any anomalous P- and S-wave velocity zones beneath TSUM (Figure 7a). At LSZ, our study indicates that the Moho is located at a depth of ~43 km (Figure 7b), which is consistent with that obtained by Midzi and Ottemöller (2001) (~40–43 km). The crustal P-wave velocity is nearly constant (~6.2 km/s) between ~8 km to 32 km depth (Figure 7b). Below ~32 km depth, P-wave velocities increase rather sharply from ~6.2 km/s to 7.8 km/s at the Moho (Figure 7b).

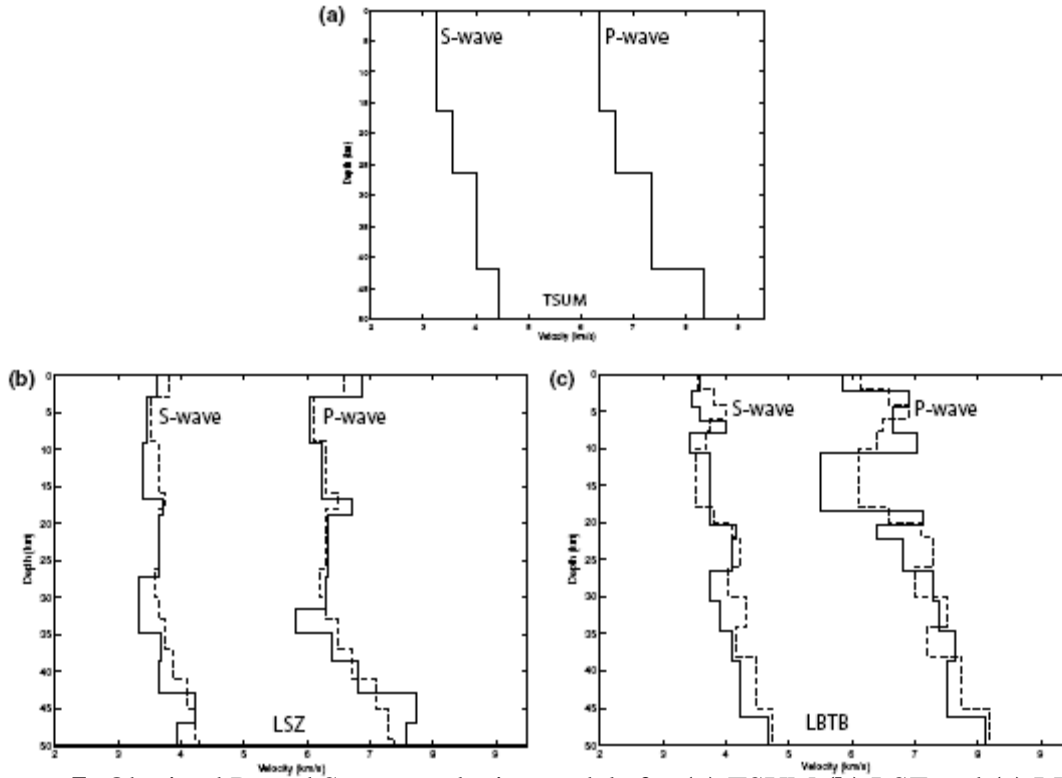


Figure 7: Obtained P- and S-wave velocity models for (a) TSUM (b) LSZ and (c) LBTB. The P- and S-wave velocity models (broken lines) in (b) and (c) are from receiver function studies by Midzi and Ottemöller (2001).

The crustal S-wave velocities range between ~3.6 km/s and 3.8 km/s (Figure 7b). We also obtain a lower crustal low-velocity zone of ~5 – 8 km thickness in our velocity model for LSZ (Figure 7b), consistent with models for seismic stations elsewhere in Africa in the cratonic regions. Such a phenomenon was also noted by Midzi and Ottemöller (2001). Figure 5k shows the P- and S-wave velocity models beneath LBTB obtained in our study. There appears to be a broad crust–mantle transition zone beneath

LBTB and the upper bound of the estimate of crustal thickness beneath LBTB is ~46 km (Figure 7c). Midzi and Ottemöller (2001) also noted the same and predicted a crust-mantle transition zone between 37-45 km. The crustal P- and S-wave velocities beneath LBTB range between 5.8 km/s–7.5 km/s, and 3.5 km/s–4.2 km/s, respectively, except for a distinct low P-velocity (5.4 km/s) zone of ~8 km thickness in the upper crust between 10 km–20 km depth (Figure 7c). Such a low-velocity zone was also obtained by Midzi and Ottemöller (2001) at similar depths, however, the P-wave velocities predicted from our study for this zone are significantly lower than those predicted by Midzi and Ottemöller (2001). Given its appearance beneath other cratonic seismic stations in Africa, the crustal low-velocity zone appears to be a general characteristic of the region.

In summary, Table 1 provides the crustal P- and S-wave velocities and depth to the Moho for each seismic station in Africa as obtained from our study.

Table 1: Summary of crustal P- and S-wave velocities and depth of the Moho beneath Africa

Station name	Station code	Range of V_p (km s ⁻¹)	Range of V_s (km s ⁻¹)	Depth of Moho (km)
Tamanrasset, Algeria	TAM	6.25–6.8	3.1–3.9	36
Dimbokro, Cote d'Ivoire	DBIC	6.5–7.3	3.7–4.7	41
Midelt, Morocco	MDT	6.2–6.4	3.4–3.7	38
M'Bour, Senegal	MBO	5.6–7.2	3.1–4.1	42
Arta Tunnel, Djibouti	ATD	4.7–7.2	2.5–4.3	21
Mount Furi, Ethiopia	FURI	5.3–6.8	3.2–3.6	39
Kilima Mbogo, Kenya	KMBO	5.4–8.0	3.5–4.5	38
Mbarara, Uganda	MBAR	6.2–7.6	2.9–4.2	36
Tsumeb, Namibia	TSUM	6.3–7.3	3.2–4.0	42
Lusaka, Zambia	LSZ	6.2–7.8	3.6–3.8	43
Lobatse, Botswana	LBTB	5.4–7.5	3.5–4.2	46

4.2 China

Based on our selection criteria, we analyzed 129 earthquakes recorded at eleven permanent broadband seismic stations in China. The number of earthquakes recorded at each station range between 3 and 31. Figure 8 shows the locations of these seismic stations and the geographical distribution of the earthquakes analyzed. The stations encompass tectonic provinces such as the north and south China blocks, Tibetan plateau, and Tien Shan Mountains. Although all the events recorded at every station have been analyzed, work is ongoing to improve some of the modeling results. Therefore in this paper, we only present examples from those stations that show good waveform matches. Figure 9 shows examples of waveform fits of data from earthquakes recorded at seismic stations LSA, WMQ, and BJT. At all the seismic stations we observe and obtain good matches between data and synthetics generated by our modeling method for the direct S, Sp, and SsPmP phases. Except the direct S phase which we observe on both the components at all the stations, we note that the Sp phase is prominent on the vertical and

radial components at LSA and WMQ but not on the radial component at BJT. Similarly, we observe the SsPmP phase on both components at LSA and WMQ but not on the radial component at BJT. However, the SPL phase is only noted and well matched on the radial component at LSA. We confirm the presence of the SPL phase by analyzing the particle motion within the corresponding time window which turns out to be prograde elliptical.

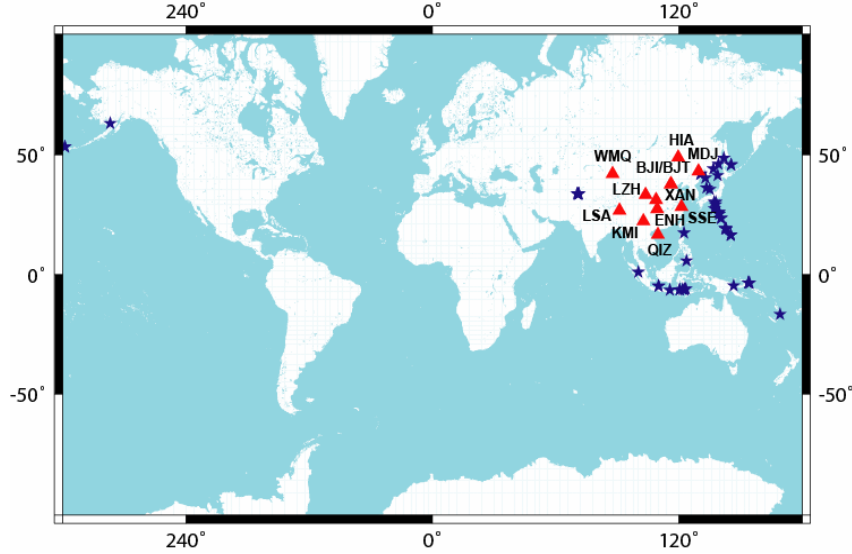


Figure 8: Map showing earthquakes analyzed in this study (blue stars) and the permanent broadband seismic stations in China (red triangles) that recorded them. The respective station codes are shown adjacent to location of each station.

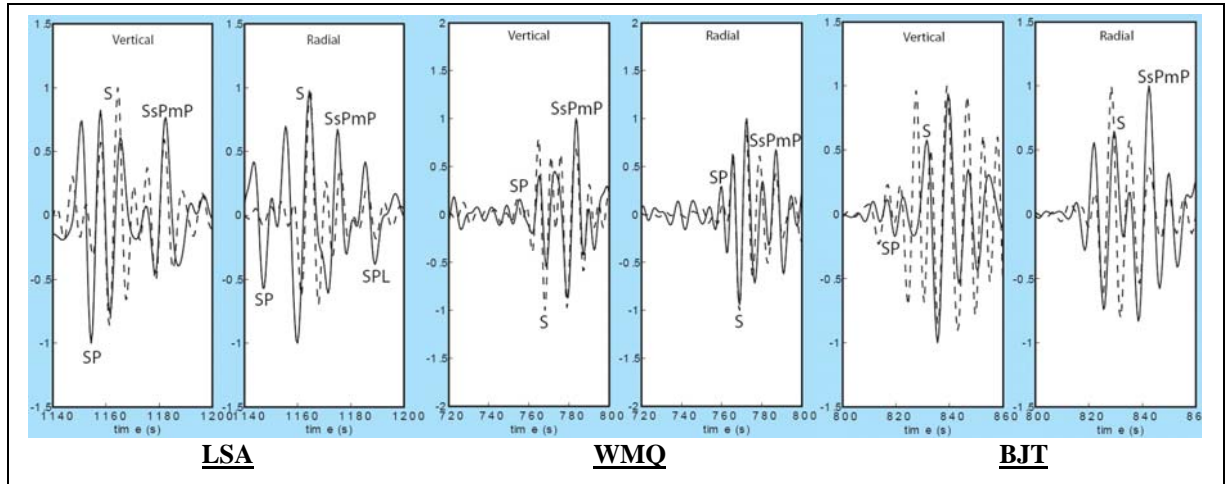


Figure 9: Vertical and radial component seismograms for example events recorded at LSA, WMQ, and BJT showing the observed (solid line) and synthetic (dashed line) waveforms. The correlated waveforms are indicated on the panels.

Based on waveform fits obtained for each source-receiver pair we generate velocity models for each seismic station. However, the models generated for the same station using waveform fits from different earthquakes recorded at that station, although similar, are not identical. To analyze which velocity model is more reliable we calculate

the PPD and correlation matrices for the modeling results of each source-receiver pair. Here, we show examples of these statistical calculations from an event recorded at LSA (Figure 10a and b), and WMQ (Figure 10c and d).

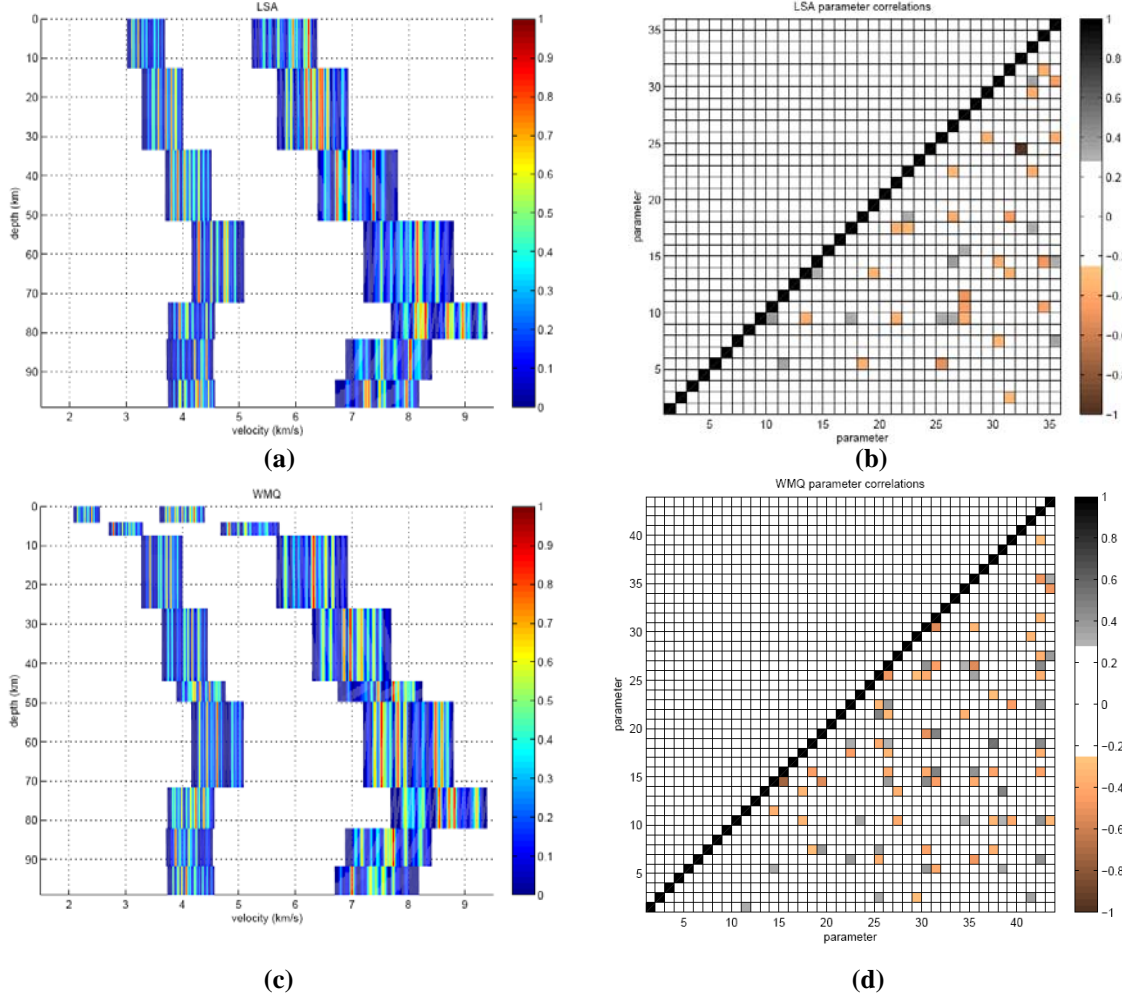


Figure 10: Posterior Probability Distribution (PPD) for example events recorded at (a) LSA and (c) WMQ. More peaked distributions indicate more uniqueness among different models and fewer trade-offs among model parameters. Model parameter correlation matrices for the same event at (b) LSA and (d) WMQ are also shown. Each small square represents a model parameter (V_p , V_s , Thickness of Layer, and Density) on both axes. The correlations range between -1 and 1. Sparse colored squares off-diagonal indicate better constraints and greater confidence (less trade-offs) in those parts of the models. Note that at LSA where we observe and match the SPL phase there are less colored squares in the correlation matrix in the lower crust-upper mantle (b) compared to that at WMQ (d), suggesting that SPL improves constraints in those parts of the models.

Finally, in Figure 11 we show the velocity models for each seismic station in China that we obtain from our modeling exercises so far. Wherever available we also show the models from an earlier study for comparison. Our models are consistent with regional tectonics and models obtained from earlier studies using receiver functions and seismic tomography. The crustal thicknesses beneath stations in north China block range

between ~32 and 42 km with the crust in central part of the block near station BJT being thicker. However, within north China block towards its western edge, the crust appears anomalously thick (~55 km) beneath station LZH. This region also coincides with the border of north China block and Tibetan plateau. The south China block consists of widely varying crustal thicknesses: ~33 km beneath station ENH in the northern part of the block and ~52 km beneath station KMI in the southern part, for example. The southern part of south China block near station KMI also coincides with its border with the Tibetan plateau, where the Moho is significantly deeper than elsewhere in China, implying a deep crustal root. Station LSA, in Lhasa, Tibet, has a crustal thickness of ~53 km. In Tien Shan Mountains in northwestern China, the crust is thicker than average (~42 km) but not as thick as that beneath the Tibetan plateau.

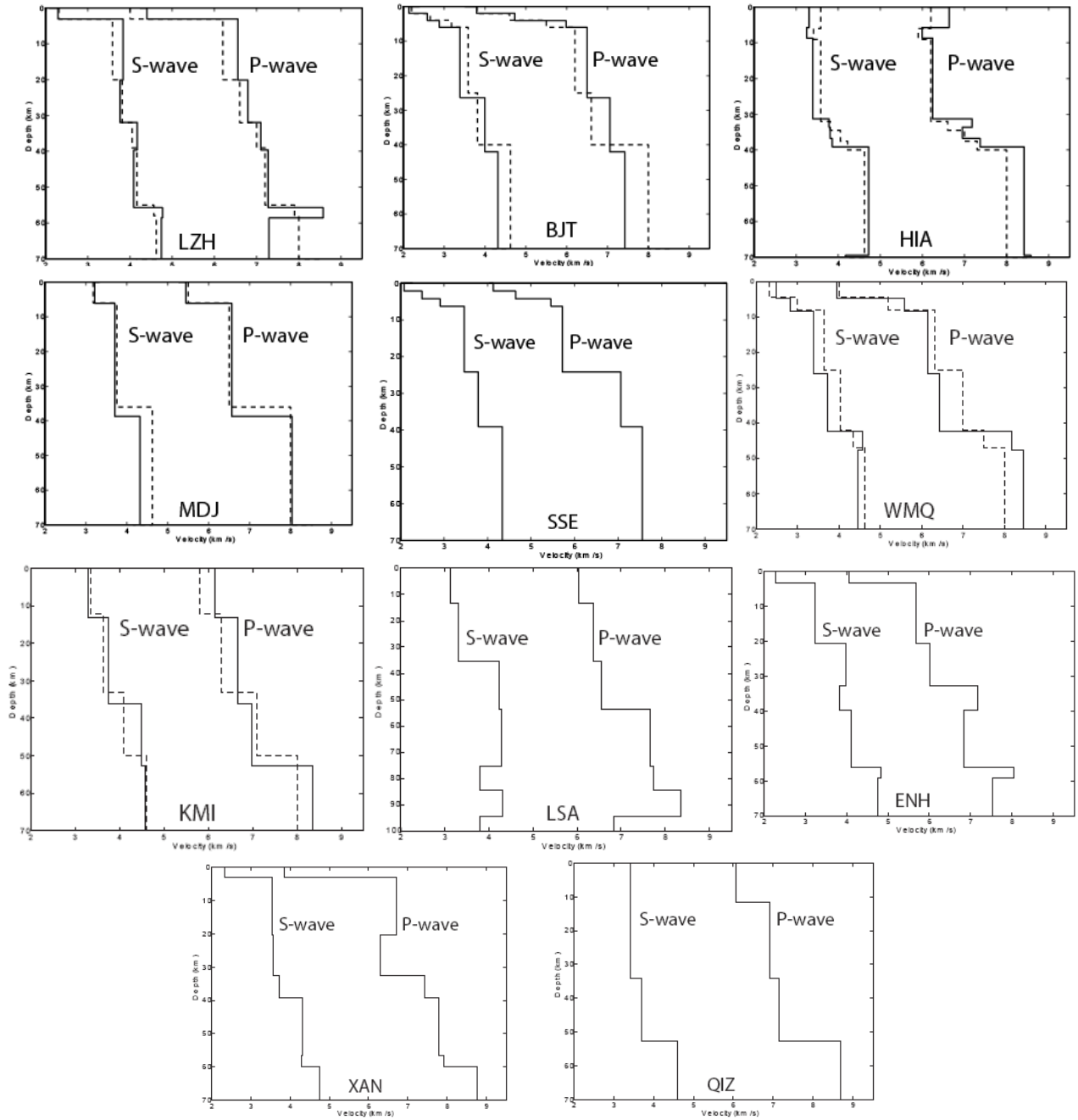


Figure 11: Obtained P- and S-wave velocity models (solid lines) for the eleven permanent broadband seismic stations in China. Station codes are indicated in each panel. The models (broken lines) in LZH, BJT, HIA, MDJ, WMQ, and KMI are from receiver function studies by Mangino et al. (1999).

In summary, Table 2 provides the crustal P- and S-wave velocities and depth to the Moho for each seismic station in China as obtained from our study.

Table 2: Summary of crustal P- and S-wave velocities and depth of the Moho beneath China

Station	Range of Vp (km/s)	Range of Vs (km/s)	Depth of Moho (km)
LZH	4.3-8.5	2.3-4.7	55
BJT	3.8-7.3	2.2-4.3	42
HIA	6.0-8.4	3.2-4.8	40
MDJ	5.4-8.0	3.2-4.3	39
WMQ	4.0-8.2	2.5-4.5	42
SSE	4.1-7.5	2.1-4.3	39 (?)
KMI	6.1-8.3	3.3-4.6	52
LSA	6.0-7.7	3.1-4.2	53
ENH	4.0-7.1	2.3-4.0	33
XAN	3.9-7.5	2.3-3.8	32
QIZ	6.0-8.7	3.4-4.6	52

(?) The depth of Moho computations are preliminary and requires assessment of uncertainties

4.3 Canada

We apply our modeling method to data from 137 earthquakes recorded teleseismically at 11 permanent broadband seismic stations spanning Canada during 1976-2005 (Figure 12). We show examples of waveform fitting for some events, and also

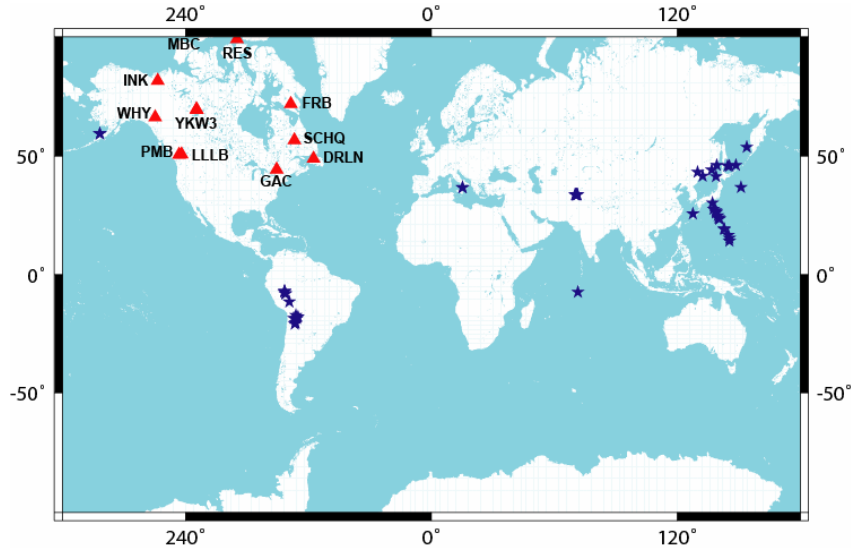


Figure 12: Map showing earthquakes analyzed in this study (blue stars) and the permanent broadband seismic stations in Canada (red triangles) that recorded them. The respective station codes are shown adjacent to location of each station.

describe interpretations of the uncertainty computations. The number of earthquakes recorded at each station range between 3 and 26. The stations encompass tectonic provinces such as Cordilleran orogen, western plains and Slave province in western Canada, Grenville province and Appalachian orogen in eastern Canada, and the Canadian Arctic. Figure 13a shows examples of waveform fits of data from earthquakes recorded at seismic stations INK, LLLB, and GAC. At all the seismic stations we observe and obtain good matches between data and synthetics of the direct S and SsPmP phases. We observe and match the Sp phase on both the components at INK but only on the vertical component at LLLB, and radial component at GAC. The SPL phase appears abundant at the Canadian seismic stations and we observe and obtain good matches on the vertical component at INK, both components at LLLB, and radial component at GAC. We confirm our observation of the SPL phase by observing prograde elliptical particle motion diagrams (Figure 13b). We also calculate the posterior probability distribution (PPD) and correlation matrix for each source-receiver pair, examples of which we show in Figure 13c. In Figure 14 we present the final velocity models for each seismic station

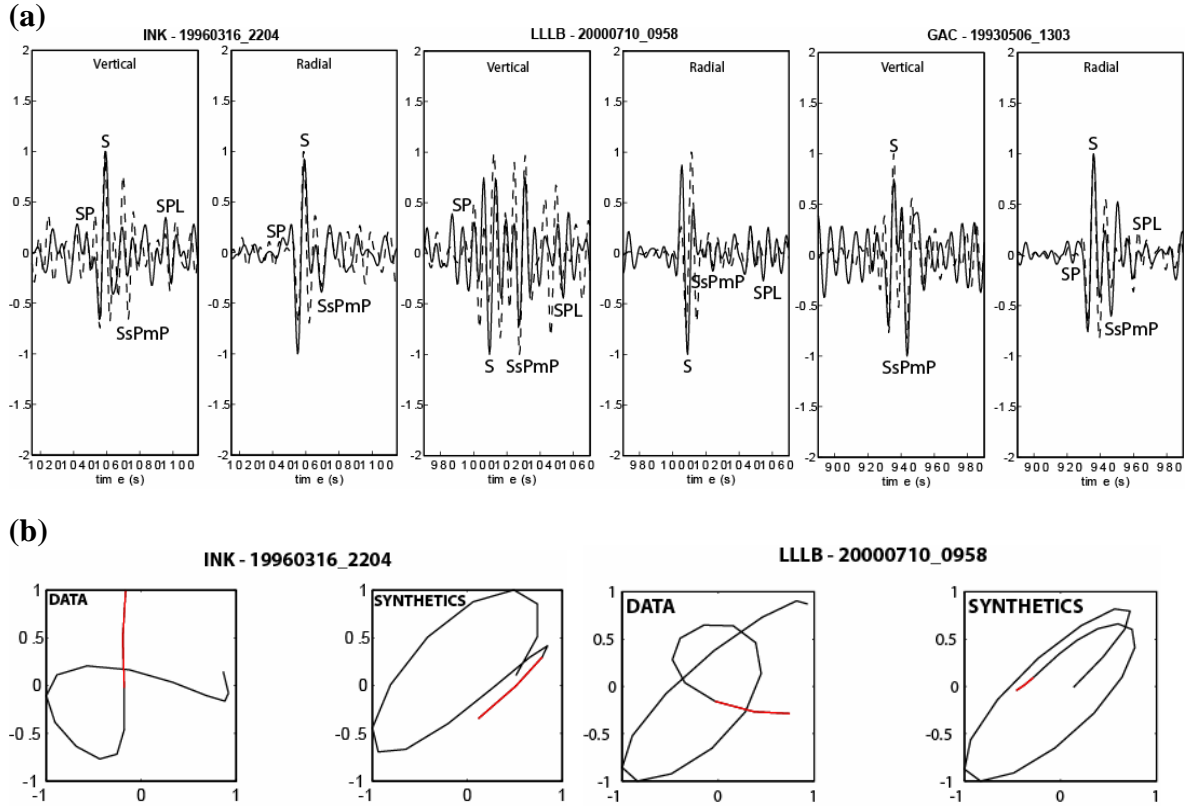


Figure 13: (a) Vertical and radial component seismograms for example events recorded at INK, LLLB, and GAC showing the observed (solid line) and synthetic (dashed line) waveforms. The correlated waveforms are indicated on the panels. (b) Particle motion diagrams for a time window of 8 seconds around the SPL phase on the data and synthetics for an event recorded at INK, and 10 seconds at LLLB and GAC showing prograde elliptical motion diagnostic of the SPL phase. The red portions of the diagrams indicate beginning of the motion.

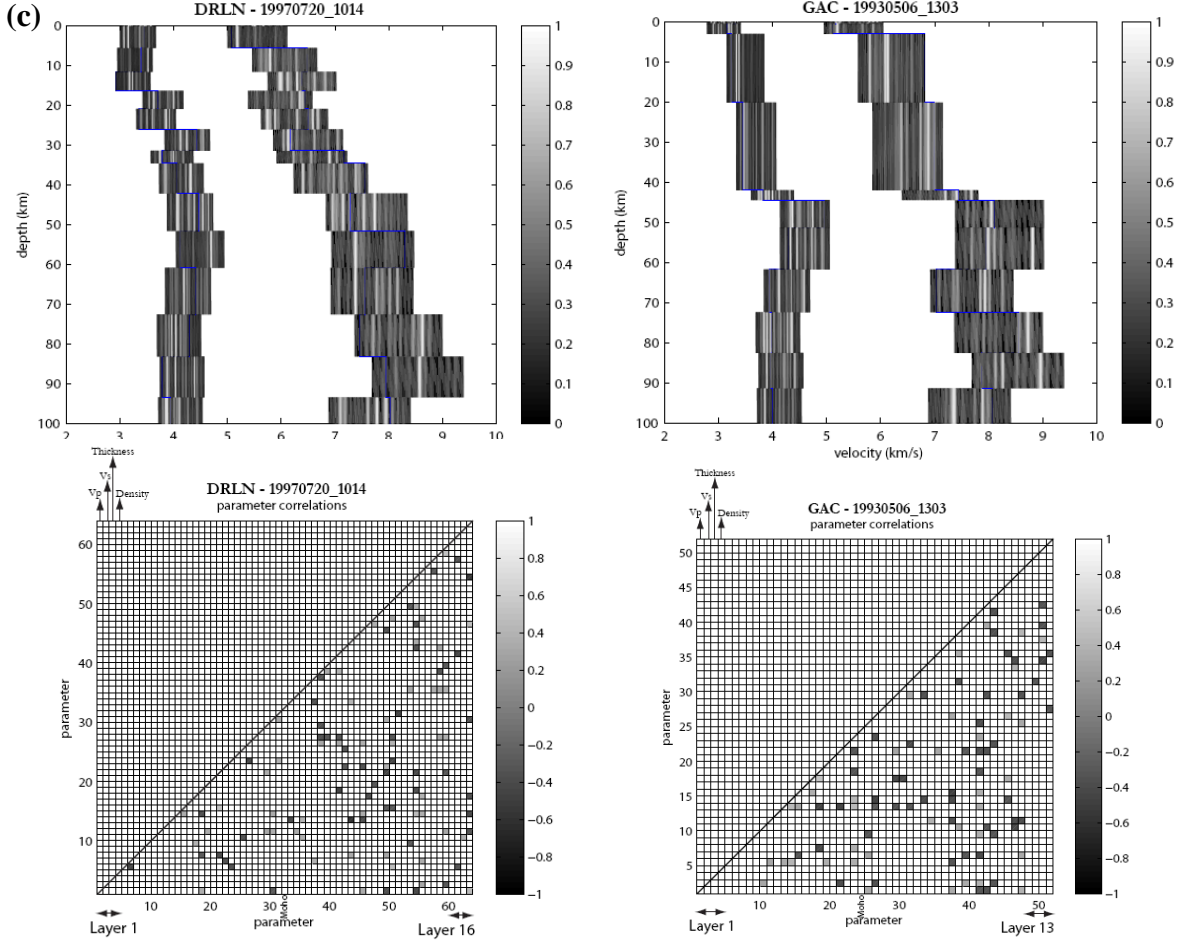


Figure 13: (c) Marginal Posterior Probability Distributions (PPD) for example events recorded at seismic stations DRLN and GAC. More peaked distributions indicate more uniqueness among different models and fewer trade-offs among model parameters. Model parameter correlation matrices for the same events at DRLN and GAC. Each small square represents a model parameter on both axes. The correlations range between -1 and 1. Sparse colored squares off-diagonal indicate better constraints and lesser trade-offs in those parts of the models.

in Canada. Wherever available, we also show the earlier velocity models (Cassidy, 1995; Darbyshire, 2003) for comparison. Our models beneath the Canadian seismic stations are consistent with earlier studies (e.g. Ramesh et al., 2002) and regional tectonics (Figure 14). Crustal thicknesses beneath stations in the northern Cordilleran orogen, western plains, and Slave province range between 35 and 37 km. The Moho appears to be slightly shallower (30-36 km) beneath stations in the southern Cordilleran orogen. In eastern Canada, the crust beneath stations of the Grenville province and Appalachian orogen is generally thick (~44 km) with the exception of that beneath station DRLN, in the northeast, where it is ~33 km. Moho depths beneath stations in the Canadian Arctic range between ~30 and 41 km. We also observe low-velocity zones in the crust and uppermost mantle at some stations, however the constraints on them are not strong. Taken together, the results provide a comprehensive snapshot of the velocity structure beneath Canada.

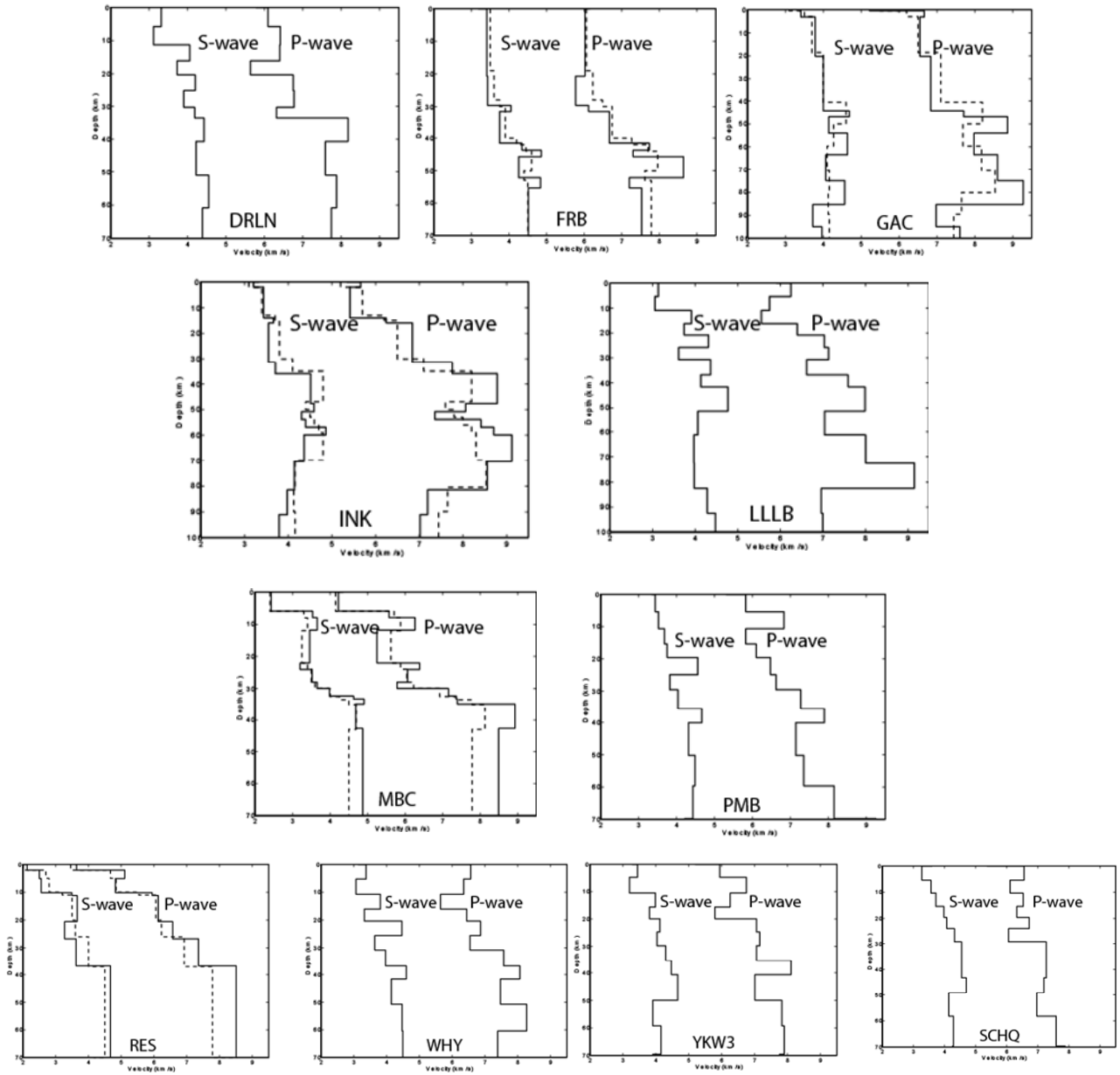


Figure 14: P- and S-wave velocity models (solid lines) for seismic stations in Canada. The P- and S-wave velocity models in FRB, MBC, and RES are from receiver function studies by Darbyshire (2003), and in GAC and INK are those from Cassidy (1995).

In summary, Table 3 provides the crustal P- and S-wave velocities, depth to the Moho, and average crustal Poisson's ratio for each seismic station in Canada as obtained from our study. (P.S. The Poisson's ratio computations are preliminary)

Table 3: Summary of crustal P- and S-wave velocities, depth of the Moho, and average crustal Poisson's ratio beneath Canada

Station	Range of Vp (km/s)	Range of Vs (km/s)	Depth of Moho (km)	Av. Crustal Poisson's Ratio
DRLN	6.1-8.1	3.3-4.3	33	0.24
FRB	6.0-7.8	3.3-4.8	41	0.25
GAC	6.5-7.6	3.4-4.6	44	0.29
INK	5.6-8.7	3.2-4.4	35	0.21
LLLB	6.2-7.5	3.2-4.3	36	0.20
MBC	4.2-7.2	2.4-4.0	30	0.22
PMB	5.8-7.9	3.4-4.6	30	0.24
RES	3.6-8.5	2.2-4.6	38	0.26
WHY	6.5-7.5	3.3-4.4	37 (?)	0.24
YKW3	6.0-8.1	3.4-4.4	35	0.24
SCHQ	6.6-7.2	3.2-4.4	31 (?)	0.27

(?) The depth of Moho computations are preliminary and requires assessment of uncertainties

5. CONCLUSIONS

In this report, we discussed a waveform fitting technique that relies on a parallelized reflectivity method to compute synthetic seismograms and implements a global optimization algorithm using Very Fast Simulated Annealing (VFSA). We also demonstrated the application of the method to determine one-dimensional, azimuthally-dependent, crust and upper mantle P- and S-wave velocity structure beneath broadband seismic stations across the continent of Africa, China, and Canada. Our technique is complementary to receiver function methods, has many of its advantages, and adds to them in providing regional crust and upper mantle structure appropriate for locating small, regional events. We are also able to compute synthetic seismograms that contain all the possible phases for a prescribed source-receiver path, and obtain direct estimates of the P- and S-wave velocities beneath seismic stations. Statistical tools incorporated in the technique allow us to assess uncertainties associated with our models and estimate tradeoffs between model parameters in different layers. The use of the SPL phase as shown in the study, enhances our constraints for lower crust and upper mantle structure beneath the seismic stations.

Advantages of the waveform modeling method described here include the ability to model simultaneously all phases that might be present in the observed waveform, provide independent estimates of both P- and S-wave velocities, assess uncertainties in model parameters, find a range of acceptable models that explain the data, and minimize

dependence of the final results on the initial model. Furthermore, a full waveform fitting procedure iterated by VFSA reduces the opportunities for imposing bias by automating the choice of model perturbations and by eliminating the need for a user to pick functionals of the seismogram (e.g., arrival time, amplitude) precisely or accurately, or to identify phases correctly and construct associated raypaths. The procedure is therefore relatively free of user bias and robust compared to methods in which one measures functionals in pre-processing steps. In our method, we avoid the risk of incorrectly identifying phases or incorrectly measuring arrival times due to wave interference or pure blunders. All phases possible for each iteration's model will be included in its corresponding synthetic seismograms (including appropriate interference and distortion), they will automatically be evaluated against the observed data without risk that mis-identification will map mis-fits to incorrect raypaths, for example.

Applied to large-magnitude, deep-focus earthquakes recorded teleseismically in Africa, China, and Canada our method successfully produced crust and upper mantle (wherever SPL was observed) P- and S-wave velocity models, that are consistent with earlier models, in the sense that they fall within the associated uncertainties we found with the products of multiple VFSA runs. For some seismic stations in Africa, our study provided such velocity models that are the first of their kind. Our models were also consistent with the broad regional tectonics of the respective regions. While the technique described here provided layered, one-dimensional models, a dataset that includes a broader azimuthal distribution of earthquakes for each station would allow this source-receiver-based technique to produce better azimuthally-dependent models, and thus a more detailed view of the Earth structure.

REFERENCES

- Ammon, C. J., Randall, G. E. & Zandt, G., 1990. On the nonuniqueness of receiver function inversions, *J. Geophys. Res.*, **95**, 15,303 – 15,318.
- Ayele, A., Stuart, G. & Kendall, J. -M., 2004. Insights into rifting from shear wave splitting and receiver functions: an example from Ethiopia, *Geophys. J. Int.*, **157**, 354 – 362.
- Baag, C. E. & Langston, C. A., 1985. Shear-coupled PL, *Geophys. J. Int.*, **80**, 363 – 385.
- Baag, C. E. & Langston, C. A., 1986. Diffracted Sp Generated Under the Australian Shield, *J. Geophys. Res.*, **91**, 9,507 – 9,516.
- Bock, G., 1988. Sp phases from the Australian upper mantle, *Geophys. J. Int.*, **94**, 73 – 81.
- Bock, G., 1991. Long-Period S To P Converted Waves And the Onset of Partial Melting Beneath Oahu, Hawaii, *Geophys. Res. Lett.*, **18**, 869 – 872.
- Bock, G. & Kind, R., 1991. A global study of S-to-P and P-to-S conversions from the upper mantle transition zone, *Geophys. J. Int.*, **107**, 117 – 129.
- Cassidy, J. F., 1995. A comparison of the receiver structure beneath stations of the Canadian National Seismic Network, *Can. J. Earth Sc.*, **32**, 938-951.
- Chander, R., Alsop, L. E. & Oliver, J., 1968. On the synthesis of shear coupled PI waves, *Bull. Seismol. Soc. Am.*, **58**, 1,849 – 1,877.
- Darbyshire, F. A., 2003. Crustal structure across the Canadian High Arctic region from teleseismic receiver function analysis, *Geophys. J. Int.*, **152**, 372-391.
- Dugda, M. T., Nyblade, A. A., Julià, J., Langston, C. A., Ammon, C. J. & Simiyu, S., 2005. Crustal structure in Ethiopia and Kenya from receiver function analysis: Implications for rift development in eastern Africa, *J. Geophys. Res.*, **110**, B01303, doi:10.1029/2004JB003065.
- Dugda, M. T. & Nyblade, A. A., 2006. New constraints on crustal structure in eastern Afar from the analysis of receiver functions and surface wave dispersion in Djibouti, in Yirgu, G., Ebinger, C. J. & Maguire, P. K. H. (eds.), *The Structure and Evolution of the East African Rift System in the Afar Volcanic Province*, *Geol. Soc. London, Special Publications*, **259**, 241 – 253.
- Dziewonski, A. M. & Anderson, D. L., 1981. Preliminary reference Earth model, *Phys. Earth planet. Int.*, **25**, 297 – 356.
- Frazer, L. N., 1977. Synthesis of shear coupled PL, Ph.D Thesis, Princeton University, Princeton, New Jersey, U.S.A., 54 pp.
- Gangopadhyay, A., Pulliam, J., Sen, M. K., (2007). Waveform Modeling of Teleseismic S, Sp, SsPmP, and Shear-Coupled PL waves for Crust and Upper Mantle Velocity Structure Beneath Africa. *Geophys. J. Int.*, **170**, 1,210 - 1,226, doi:10.1111/j.1365-246X.2007.03470.x.
- Gropp, W. & Lusk, E., 1995. Dynamic process management in an MPI setting, *7th IEEE Symposium on Parallel and Distributed Processing*, p. 530.
- Hazler, S. E., Sheehan, A. F., McNamara, D. E. & Walter, W. R., 2001. One-dimensional Shear Velocity Structure of Northern Africa from Rayleigh Wave Group Velocity Dispersion, *Pageoph.*, **158**, 1,475 – 1,493.
- Ingber, L., 1989. Very fast simulated reannealing, *Mathl. Comput. Modeling*, **12**, 967 – 993.

- Jordan, T. H. & Frazer, L. N., 1975. Crustal and upper mantle structure from Sp phases, *J. Geophys. Res.*, **80**, 1,504 – 1,518.
- Julià, J., Ammon, C. J., Herrmann, R. B. & Correig, A. M., 2000. Joint Inversion of Receiver Function and Surface Wave Dispersion Observations, *Geophys. J. Int.*, **143**, 99 – 112.
- Kennett, B. L. N., 1983. Seismic wave propagation in stratified media, Cambridge University Press, Cambridge, 338 pp.
- Langston, C. A., 1996. The SsPmP Phase in Regional Wave Propagation, *Bull. Seismol. Soc. Am.*, **86**, 133 – 143.
- Mallick, S. & Frazer, L. N., 1987. Practical aspects of reflectivity modeling, *Geophysics*, **52**, 1,355 – 1,364.
- Mangino, S., Priestley, K. & Ebel, J., 1999. The Receiver structure beneath the China Digital Seismograph stations, *Bull. Seis. Soc. Am.*, **89**, 1,053-1,076.
- Marone, F., van der Meijde, M., van der Lee, S. & Giardini, D., 2003. Joint inversion of local, regional and teleseismic data for crustal thickness in the Eurasia-Africa plate boundaryregion, *Geophys. J. Int.*, **154**, 499 – 514.
- Midzi, V. & Ottemöller, L., 2001. Receiver function structure beneath three southern Africa seismic broadband stations, *Tectonophysics*, **339**, 443 – 454.
- Oliver, J., 1961. On the long period character of shear waves, *Bull. Seismol. Soc. Am.*, **51**, 1 – 12.
- Owens, T. J., Zandt, G. & Taylor, S. R., 1984. Seismic evidence for an ancient rift beneath the Cumberland Plateau, Tennessee: A detailed analysis of broadband teleseismic P waveforms, *J. Geophys. Res.*, **89**, 7,783 – 7,795.
- Owens, T. J. & Zandt, G., 1997. Implications of crustal property variations for models of Tibetan plateau evolution, *Nature*, **387**, 37 – 43.
- Pasyanos, M. E. & Walter, W. R., 2002. Crust and upper-mantle structure of North Africa, Europe and the Middle east from inversion of surface waves, *Geophys. J. Int.*, **149**, 463 – 481.
- Pasyanos, M. E., Walter, W. R., Flanagan, M. P., Goldstein, P. & Bhattacharyya, J., 2004. Building and Testing an *a priori* Geophysical Model for Western Eurasia and North Africa, *Pageoph.*, **161**, 235 – 281.
- Pasyanos, M. E., 2005. A variable resolution surface wave dispersion study of Eurasia, North Africa, and surrounding regions, *J. Geophys. Res.*, **110**, B12301, doi:10.1029/2005JB003749.
- Pulliam, J., Sen, M. K., Frohlich, C. & Grand, S., 2002. Waveform Modeling of the Crust and Upper Mantle Using S, Sp, SsPmP and Shear-Coupled PL waves, *Proc. 24th Seis. Res. Rev. – Nuclear Explosion Monitoring: Innovation and Integration*, 144 – 153.
- Pulliam, J. & Sen, M., 2004. Waveform Modeling of the Crust and Upper Mantle using S, Sp, SsPmP, and Shear-Coupled PL waves for improved event location, focal depth determination, and uncertainty estimation, *Proc. 26th Seis. Res. Rev. – Trends in Nuclear Explosion Monitoring*, 142 – 152.
- Pulliam, J. & Sen, M. K., 2005. Assessing Uncertainties in Waveform Modeling of the Crust and Upper Mantle, *Proc. 27th Seis. Res. Rev. – Ground-Based Nuclear Explosion Monitoring Technologies*, 152 – 160.

- Ramesh, D. S., Kind, R. & Yuan, X., 2002. Receiver function analysis of the North American crust and upper mantle, *Geophys. J. Int.*, **150**, 91 – 108.
- Sandvol, E., Seber, D., Calvert, A. & Barazangi, M., 1998. Grid search modeling of receiver functions: Implications for crustal structure in the Middle East and North Africa, *J. Geophys. Res.*, **103**, 26,899 – 26,917.
- Sen, M. K. & Stoffa, P. L., 1991. Non-linear one-dimensional seismic waveform inversion using simulated annealing, *Geophysics*, **56**, 1624 - 1638.
- Sen, M. K. & Stoffa, P. L., 1995. Global Optimization Methods in Geophysical Inversion, Elsevier Science Publishing Company, The Netherlands, 281 pp.
- Sen, M. K. & Stoffa, P. L., 1996. Bayesian inference, Gibbs' sampler and uncertainty estimation in geophysical inversion, *Geophysical Prospecting*, **44**, 313 - 350.
- Swenson, J. L., Beck, S. L. & Zandt, G., 1999. Regional distance shear-coupled *PL* propagation within the northern Altiplano, central Andes, *Geophys. J. Int.*, **139**, 743 – 753.
- Tarantola, A., 1994. Inverse Problem Theory: Methods for Data Fitting and Model Parameter Estimation, Elsevier, Amsterdam, The Netherlands, 600 pp.
- Tiberi, C., Ebinger, C., Ballu, V., Stuart, G. & Oluma B., 2005. Inverse models of gravity data from the Red Sea – Aden – East African rifts triple junction zone, *Geophys. J. Int.*, **163**, 775 – 787.
- Wessel, P. & Smith, W. H. F., 1991. Free software helps map and display data, *EOS Trans. AGU*, **72**, 441.
- Zandt, G. & Randall, G. E., 1985. Observations of Shear-Coupled P Waves, *Geophys. Res. Lett.*, **12**, 565 – 568.
- Zandt, G., Beck, S. L., Ruppert, S. R., Ammon, C. J., Rock, D., Minaya, E., Wallace, T. C. & Silver, P. G., 1996. Anomalous Crust of the Bolivian Altiplano, Central Andes: Constraints from Broadband Regional Seismic Waveforms, *Geophys. Res. Lett.*, **23**, 1,159 – 1,162.
- Zhang, J. & Langston, C. A., 1996. Array Observations of the Shear-Coupled *PL* Wave, *Bull. Seismol. Soc. Am.*, **86**, 538 – 543.
- Zhao, L. –S. & Frohlich, C., 1996. Teleseismic body-waveforms and receiver structures beneath seismic stations, *Geophys. J. Int.*, **146**, 525 – 540.
- Zhao, L. –S., Sen, M. K., Stoffa, P. L. & Frohlich, C., 1996. Application of very fast simulated annealing to the determination of the crustal structure beneath Tibet, *Geophys. J. Int.*, **125**, 355 – 370.

List of Symbols, Abbreviations, and Acronyms

IRIS	Incorporated Research Institutions for Seismology
GMT	Generic Mapping Tools
VFSA	Very Fast Simulated Annealing
PREM	Preliminary Reference Earth Model
SPL	Shear-Coupled PL
MPI	Message Passing Interface
SA	Simulated Annealing
PPD	Posterior Probability Density
CMT	Centroid Moment Tensor

